

RECEIVED: February 4, 2022

REVISED: August 23, 2022

ACCEPTED: September 7, 2022

PUBLISHED: September 20, 2022

Lepton flavor violation and scotogenic Majorana neutrino mass in a Stueckelberg $U(1)_X$ model

Chuan-Hung Chen,^{a,b} Cheng-Wei Chiang,^{c,b} Takaaki Nomura^d and Chun-Wei Su^c

^a*Department of Physics, National Cheng-Kung University,
Tainan 70101, Taiwan*

^b*Physics Division, National Center for Theoretical Sciences,
Taipei 10617, Taiwan*

^c*Department of Physics and Center for Theoretical Physics, National Taiwan University,
Taipei 10617, Taiwan*

^d*College of Physics, Sichuan University,
Chengdu 610065, China*

E-mail: physchen@mail.ncku.edu.tw, chengwei@phys.ntu.edu.tw,
nomura@scu.edu.cn, r10222026@ntu.edu.tw

ABSTRACT: We construct a scotogenic Majorana neutrino mass model in a gauged $U(1)_X$ extension of the standard model, where the mass of the gauge boson and the unbroken gauge symmetry, which leads to a stable dark matter (DM), can be achieved through the Stueckelberg mechanism. It is found that the simplest version of the extended model consists of the two inert-Higgs doublets and one vector-like singlet fermion. In addition to the Majorana neutrino mass, we study the lepton flavor violation (LFV) processes, such as $\ell_i \rightarrow \ell_j \gamma$, $\ell_i \rightarrow 3\ell_j$, $\mu - e$ conversion rate in nucleus, and muonium-antimuonium oscillation. We show that the sensitivities of $\mu \rightarrow 3e$ and $\mu - e$ conversion rate designed in Mu3e and COMET/Mu2e experiments make both decays the most severe constraints on the $\mu \rightarrow e$ LFV processes. It is found that $\tau \rightarrow \mu \gamma$ and $\tau \rightarrow 3\mu$ can reach the designed significance level of Belle II. In addition to explaining the DM relic density, we also show that the DM-nucleon scattering cross section can satisfy the currently experimental limit of DM direct detection.

KEYWORDS: Lepton Flavour Violation (charged), Models for Dark Matter, Neutrino Mixing, New Gauge Interactions

ARXIV EPRINT: [2201.10759](https://arxiv.org/abs/2201.10759)

Contents

1	Introduction	1
2	The model	3
2.1	Scalar masses and mixings, and Yukawa couplings	3
2.2	$U(1)_X$ Stueckelberg gauge couplings	6
3	Neutrino mass, lepton-flavor violation, kinetic mixing of gauge boson	7
3.1	Scotogenic neutrino mass matrix	7
3.2	Radiative lepton decay $\ell_i \rightarrow \ell_j \gamma$	8
3.3	$\ell_i \rightarrow 3\ell_j$ from penguin and box diagrams	10
3.4	$\mu - e$ conversion in nuclei and muonium-antimuonium oscillation	12
3.5	Loop-induced kinetic mixing between $U(1)_Y$ and $U(1)_X$	14
4	Numerical analysis	15
4.1	Inputs and constraints	15
4.2	Correlations among the LFV processes	16
4.3	DM relic density and DM-nucleon scattering cross section	21
4.4	Signatures at the LHC	25
5	Summary and discussions	26

1 Introduction

A scotogenic mechanism, which generates the neutrino mass radiatively, was proposed in ref. [1] and is referred to as the Ma model hereinafter. The model not only resolves the origin of neutrino mass but also provides a way to explain the dark matter (DM) relic density, where the current value observed by Planck collaboration is $\Omega_{\text{DM}} h^2 = 0.120 \pm 0.001$ [2].

Since the active neutrinos and the charged leptons form $SU(2)_L$ doublets in the standard model (SM), the mechanism proposed to explain the neutrino mass usually also induces interesting phenomena with lepton flavor violation (LFV), such as $\mu \rightarrow e \gamma$, $\mu \rightarrow 3e$, $\mu - e$ conversion in nuclei, and muonium-antimuonium oscillation, that are highly suppressed in the SM.

Due to their high sensitivities to new physics effects, many ongoing or planning experiments are designed to achieve unprecedented precision to study the LFV processes. For instance, the branching ratio (BR) for the $\mu \rightarrow e \gamma$ decay in MEG II experiment can reach the sensitivity of 6×10^{-14} [3]; $BR(\mu \rightarrow 3e) \lesssim 10^{-16}$ is expected in Mu3e experiment [4]; the $\mu - e$ conversion rate in COMET at J-PARC [5] and Mu2e at FNAL [6] can reach the level of $10^{-17} - 10^{-18}$, whereas the PRISM/PRIME experiment will push the conversion

rate down below 10^{-18} [7]; and the probability of muonium-antimuonium conversion in the new generation experiment with the sensitivity of $\mathcal{O}(10^{-14})$ is proposed by the MACE collaboration at CSNC [8].

In order to explain the observed neutrino mass and DM relic density and to generate testable LFV processes in a scotogenic model, we study a gauged $U(1)_X$ extension of the SM, where only the newly introduced particles carry the $U(1)_X$ charges. The neutrino mass then arises from the quantum corrections where the particles carrying the $U(1)_X$ charges are running in the loops. The DM candidate is stable if the $U(1)_X$ gauge symmetry is unbroken. However, the unbroken $U(1)_X$ would normally leads to a massless dark photon (Z') and, thus, the DM relic density may not be correctly reproduced through the resonant Z' production when we focus on the minimal extension of the SM. To guarantee the coexistence of a massive Z' gauge boson and gauge invariance, we consider the Stueckelberg mechanism by introducing a Stueckelberg scalar field instead of the mechanism of spontaneous symmetry breaking.

Using the scotogenic model to radiatively generate the Dirac neutrino mass in the Stueckelberg mechanism was studied in ref. [9]. In this work, using a different framework, we construct a model that can induce the Majorana neutrino mass. To retain the $U(1)_X$ gauge anomaly-free, we use a vector-like singlet Dirac fermion ($N_{L,R}$) instead of the right-handed singlet Majorana fermion in the Ma model. Utilizing the unbroken $U(1)_X$ gauge symmetry to stabilize DM is done at the cost of introducing two inert-Higgs doublets. Because the two inert-Higgs doublets ($\eta_{1,2}$) carry the lepton number and different $U(1)_X$ charges, lepton number violation (LNV) for generating the Majorana neutrino mass arises from the quartic coupling $(H^\dagger \eta_1)(H^\dagger \eta_2)$ in the scalar potential. In addition, since the Yukawa couplings to the SM lepton can have different structures, such as $\bar{L} N_R \tilde{\eta}_1$ and $\bar{L}^C N_L \tilde{\eta}_2$, it is found that the neutrino data can be fitted with only one generation $N_{L,R}$.

When the neutrino oscillation data and the upper limits on LFV processes are taken into account, it is found that the $\mu - e$ conversion rate and the $\mu \rightarrow 3e$ decay will exclude most of the parameter space that leads to $BR(\mu \rightarrow e\gamma) \sim \mathcal{O}(10^{-15})$, where the former is mediated by the photon-penguin diagrams and the latter is dominated by the box diagrams in the model, respectively. In other words, both experiments will give the strongest constraints on new physics for the $\mu \rightarrow e$ LFV processes. In addition, the resulting $BR(\tau \rightarrow \mu\gamma)$ and $BR(\tau \rightarrow 3\mu)$ can reach the significant levels of $\mathcal{O}(10^{-9})$ and $\mathcal{O}(10^{-10})$, respectively, as expected to probe by Belle II experiment [11].

Two sources can contribute to the DM relic density in the model. One is through the Yukawa couplings and the other arises from the gauge coupling of the kinetic mixing. The kinetic mixing between Z' and the gauge field of $U(1)_Y$ can be induced via quantum corrections; thus, the Z' gauge boson can couple to the SM particles. The singlet fermion N , which is the DM candidate in the model, can then annihilate into the SM particles through the Z' -mediated s-channel process $NN \rightarrow Z' \rightarrow F\bar{F}$ and the N -mediated t-channel one $NN \rightarrow Z'(\rightarrow F\bar{F})Z'(\rightarrow F'\bar{F}')$, where $F(F')$ denotes possible SM particles. We will demonstrate that in addition to the Yukawa coupling scenario, the induced Z' gauge coupling one can also explain the DM relic density $\Omega_{\text{DM}} h^2$. Moreover, the Z' couplings to quarks will contribute to the DM-nucleon scattering. It is found that the resulting DM-

	$SU(2)_L$	$U(1)_Y$	$U(1)_X$	Lepton #	R_p
N	1	0	Q_X	0	-1
η_1	2	1	Q_X	1	-1
η_2	2	1	$-Q_X$	1	-1

Table 1. Representations and charged assignments of new particles.

nucleon scattering cross section is under the current upper bound of direct search of DM from the XENON1T experiment [10].

The structure of this paper is organized as follows. We introduce the model and derive the relevant scalar couplings, Yukawa couplings, and Z' gauge couplings in section 2. In section 3, we formulate the phenomena for neutrino mass and LFV processes. Section 4 contains the detailed numerical analysis. Finally, we summarize our findings of the study in section 5.

2 The model

To obtain the Majorana mass for neutrinos through radiative corrections in a scotogenic $U(1)_X$ Stueckelberg gauge model, we find that a minimal extension of the SM is to include one singlet vector-like fermion N and two new inert scalar doublets $\eta_{1,2}$, where their representations and charge assignments are given in table 1. Note that here we use the convention that the electromagnetic charge $Q = T_L^3 + Y/2$. To break the lepton number in the scalar sector, $\eta_{1,2}$ need to carry one unit of lepton number while the singlet vector-like fermion has no lepton number. As a result, the new particles are R -parity odd and the SM particles are R -parity even, where the R -parity quantum number is defined as $R_p = (-1)^{3B+L+2S}$, with B , L , and S bring the baryon number, lepton number, and spin of the particle, respectively. Due to the odd R -parity property, N and the neutral components in $\eta_{1,2}$ can be DM candidates. Based upon the charge assignments, in the following we discuss the relevant Yukawa and gauge couplings for the phenomenological analysis.

2.1 Scalar masses and mixings, and Yukawa couplings

Apart from the Yukawa couplings, the most important effect to generate the Majorana mass from the scotogenic mechanism is the appearance of LNV term in the scalar potential, which dictates the scalar masses, couplings, and mixings. To examine these effects in the model, we write the scalar potential for the SM Higgs H and $\eta_{1,2}$ as:

$$\begin{aligned}
V &= V_{\text{SM}} + V(H, \eta_1, \eta_2), \\
V_{\text{SM}} &= -\mu_H^2 H^\dagger H + \lambda_H (H^\dagger H)^2, \\
V(H, \eta_1, \eta_2) &= \mu_1^2 \eta_1^\dagger \eta_1 + \mu_2^2 \eta_2^\dagger \eta_2 + \lambda_1 (\eta_1^\dagger \eta_1)^2 + \lambda_2 (\eta_2^\dagger \eta_2)^2 + \lambda_3 (\eta_1^\dagger \eta_1) (\eta_2^\dagger \eta_2) \\
&\quad + \lambda_4 (\eta_1^\dagger \eta_2) (\eta_2^\dagger \eta_1) + \left(\lambda_5 (H^\dagger \eta_1) (H^\dagger \eta_2) + \text{H.c.} \right) + \lambda_6 (H^\dagger \eta_1) (\eta_1^\dagger H) \\
&\quad + \lambda_7 (H^\dagger \eta_2) (\eta_2^\dagger H) + \lambda_8 (H^\dagger H) (\eta_1^\dagger \eta_1) + \lambda_9 (H^\dagger H) (\eta_2^\dagger \eta_2).
\end{aligned} \tag{2.1}$$

It can be seen that the only non-self-Hermitian term comes from the λ_5 term, which violates the lepton number by two units and plays an important role on the radiative generation of the Majorana neutrino mass. The tiny neutrino mass can be achieved when $\lambda_5 \ll 1$, which is the same as that shown in the Ma model [1]. For spontaneously breaking the electroweak gauge symmetry, we take $\mu_H^2, \lambda_H > 0$ as in the SM. The masses of $\eta_{1,2}$ can be irrelevant to the electroweak symmetry breaking, and we thus require $\mu_{1,2}^2(\lambda_{1,2}) > 0$. To preserve the $U(1)_X$ and R_p symmetries, the vacuum expectation values (VEVs) of $\eta_{1,2}$ have to vanish. We note that $\mu_{1,2}^2$ can in general flip sign from positive to negative via the renormalization group running effects when the mass of the vector-like singlet fermion is much heavier than the masses of inert scalar bosons and the Yukawa couplings are of $O(1)$ [12]. Since the singlet Dirac fermion is the DM candidate and its mass is smaller than the masses of inert scalar bosons, our $\mu_{1,2}^2$ are exempt from the undesirable radiative corrections. We therefore parametrize the components of the three doublet scalars as:

$$H = \begin{pmatrix} G^+ \\ \frac{1}{\sqrt{2}}(v + h + iG^0) \end{pmatrix}, \quad \eta_j = \begin{pmatrix} \eta_j^+ \\ \frac{1}{\sqrt{2}}(s_j + ia_j) \end{pmatrix}, \quad (2.2)$$

where $G^{\pm,0}$ are the Goldstone bosons, v is the VEV of H , and h is the SM Higgs boson.

Since η_1 and η_2 carry different $U(1)_X$ charges, the charged scalars η_1^\pm and η_2^\pm do not mix and their masses are respectively obtained as:

$$\begin{aligned} m_{\eta_1^\pm}^2 &= \mu_1^2 + \frac{\lambda_8 v^2}{2}, \\ m_{\eta_2^\pm}^2 &= \mu_2^2 + \frac{\lambda_9 v^2}{2}. \end{aligned} \quad (2.3)$$

Unlike the charged scalars, the neutral components of $\eta_{1,2}$ can mix via the λ_5 term. According to the scalar potential with eq. (2.2), the mass-square matrices for (s_1, s_2) and (a_1, a_2) are respectively:

$$m_S^2 = \begin{pmatrix} m_{s_1}^2 & m_{12}^2 \\ m_{12}^2 & m_{s_2}^2 \end{pmatrix}, \quad m_A^2 = \begin{pmatrix} m_{s_1}^2 & -m_{12}^2 \\ -m_{12}^2 & m_{s_2}^2 \end{pmatrix}, \quad (2.4)$$

with

$$\begin{aligned} m_{s_1}^2 &= \mu_1^2 + \frac{v^2}{2}(\lambda_6 + \lambda_8), \\ m_{s_2}^2 &= \mu_2^2 + \frac{v^2}{2}(\lambda_7 + \lambda_9), \\ m_{12}^2 &= \frac{v^2}{2}\lambda_5. \end{aligned} \quad (2.5)$$

Each of the two 2×2 mass-square matrices can be diagonalized by the corresponding orthogonal matrix $O(\theta_\xi)$ ($\xi = S, A$) through $O(\theta_\xi)m_\xi^2 O^T(\theta_\xi)$, where the $O(\theta_\xi)$ matrix can be parametrized as:

$$O(\theta_\xi) = \begin{pmatrix} \cos \theta_\xi & \sin \theta_\xi \\ -\sin \theta_\xi & \cos \theta_\xi \end{pmatrix}. \quad (2.6)$$

Since the matrix elements in m_A^2 are the same as those in m_S^2 except the sign change in the off-diagonal elements, we therefore take $\theta_S = -\theta_A \equiv \theta$. The eigenvalues for m_S^2 are found to be:

$$m_{S_{1,2}}^2 = \frac{1}{2} \left[m_{s_1}^2 + m_{s_2}^2 \pm \sqrt{(m_{s_2}^2 - m_{s_1}^2)^2 - 4(m_{12}^4)} \right]. \quad (2.7)$$

For the physical pseudoscalars $A_{1,2}$, we have $m_{A_{1(2)}}^2 = m_{S_{1(2)}}^2$. The mixing angle θ is given by:

$$\sin(2\theta) = -\frac{\lambda_5 v^2}{m_{S_2}^2 - m_{S_1}^2}. \quad (2.8)$$

Because S_i and A_i are degenerate in mass, if one of them is the DM candidate, the large gauge interaction $A_i - S_i - Z$ will render too large a DM-nucleon scattering cross section. Hence, the possibility of using a scalar as the DM candidate in this model is excluded by the direct detection experiments. Instead, the singlet vector-like fermion N becomes a promising DM candidate in the model. Since λ_5 term violates the lepton number and eventually leads to the Majorana mass, its value has to be sufficiently small, $\lambda_5 \ll 1$ [1], as alluded to earlier. As a result, the off-diagonal mass matrix element $|m_{12}^2|$ is suppressed and the mixing angle $\theta \ll 1$. In order to make the Yukawa couplings sufficiently large so that the LFV processes can be possibly detectable in the ongoing and planning experiments, we follow the approach in [13] and take $\lambda_5 = 10^{-9}$.

According to the $U(1)_X$ charges listed in table 1, the Yukawa couplings of $\eta_{1,2}$ and N to the SM leptons are given by:

$$-\mathcal{L}_Y = \bar{L} \mathbf{y}_1 \tilde{\eta}_1 N_R + \bar{L} \mathbf{y}_2 \tilde{\eta}_2 N_L^C + m_N \bar{N}_L N_R + \text{H.c.}, \quad (2.9)$$

where the flavor indices are suppressed, $L^T = (\nu_\ell, \ell)$ denotes the left-handed lepton doublet in the SM, $\tilde{\eta}_j = i\tau_2 \eta_j^*$ with τ_2 being a Pauli matrix, $N^C = C\gamma_0 N^*$ is the charge conjugation of N , and m_N is the mass of N . Although $\mathbf{y}_{1,2}$ can be generally complex, we can rotate away the phase of one of them by redefining the phases of the complex lepton doublet L . In our following analysis, we take the convention that \mathbf{y}_1 is real and \mathbf{y}_2 is complex, as parametrized by $y_{2k} = |y_{2k}|e^{i\phi_k}$ ($k = 1, 2, 3$). Using eqs. (2.2) and (2.6), the Yukawa couplings in eq. (2.9) can be decomposed as:

$$\begin{aligned} -\mathcal{L}_Y = & -\bar{\ell}_L \mathbf{y}_1 N_R \eta_1^- - \bar{\ell}_L \mathbf{y}_2 N_L^C \eta_2^- + m_N \bar{N}_L N_R \\ & + \frac{1}{\sqrt{2}} \bar{\nu}_{\ell L} \mathbf{y}_1 N_R [c_\theta(S_1 - iA_1) - s_\theta(S_2 + iA_2)] \\ & + \frac{1}{\sqrt{2}} \bar{\nu}_{\ell L} \mathbf{y}_2 N_L^C [s_\theta(S_1 + iA_1) + c_\theta(S_2 - iA_2)] + \text{H.c.}, \end{aligned} \quad (2.10)$$

where we denote c_θ (s_θ) $\equiv \cos \theta$ ($\sin \theta$). We note that if we take the charged lepton ℓ_L as the mass eigenstate, in general, the $\eta_{1,2}^\pm$ Yukawa couplings are modified as $V_L^\ell \mathbf{y}_i$, where V_L^ℓ is a unitary matrix introduced for diagonalizing the charged lepton mass matrix. Therefore, the Yukawa couplings of η_i^\pm are generally different from those of S_i and A_i . Since we know nothing about the information of V_L^ℓ in the SM, we adopt $V_L^\ell = 1$ to reduce the number of free parameters in the study. As a result, the effects contributing to the neutrino mass through the Yukawa couplings of S_i and A_i now have a strong correlation to the LFV processes that are mediated by η_i^\pm .

2.2 $U(1)_X$ Stueckelberg gauge couplings

The Lagrangian invariant under the $SU(2)_L \times U(1)_Y \times U(1)_X$ gauge symmetry with the Stueckelberg gauge field included is given by:

$$\begin{aligned} \mathcal{L}_{\text{kin}} = & -\frac{1}{4}\vec{W}_{\mu\nu} \cdot \vec{W}^{\mu\nu} - \frac{1}{4}\hat{B}_{\mu\nu}\hat{B}^{\mu\nu} - \frac{1}{4}\hat{Z}'_{\mu\nu}\hat{Z}'^{\mu\nu} + \frac{m_{Z'}^2}{2}\left(\hat{Z}'^\mu - \frac{1}{m_{Z'}}\partial^\mu B\right)^2 \\ & - \frac{1}{2\beta}\left(\partial_\mu\hat{Z}'^\mu + m_{Z'}\beta B\right)^2 + \bar{N}i\not{D}N + (D_\mu\eta_1)^\dagger(D^\mu\eta_1) + (D_\mu\eta_2)^\dagger(D^\mu\eta_2), \end{aligned} \quad (2.11)$$

where $W_{\mu\nu}^i$, $\hat{B}_{\mu\nu}$, and $\hat{Z}'_{\mu\nu}$ are the gauge field stress tensors associated with the $SU(2)_L$, $U(1)_Y$, and $U(1)_X$ gauge groups, respectively, B field is the Stueckelberg scalar field, β is the gauge fixing parameter, and $m_{Z'}$ is the mass of $U(1)_X$ Stueckelberg gauge field. We note that the kinetic mixing term $\hat{B}_{\mu\nu}\hat{Z}'^{\mu\nu}$ can be rotated away by redefining the gauge fields \hat{B}_μ and \hat{Z}'_μ . However, we will show later that the mixings in γ - Z' and Z - Z' can be induced through radiative corrections.

The covariant derivatives on N and η_i are expressed as:

$$\begin{aligned} D_\mu N &= (\partial_\mu + ig_X q_N \hat{Z}'_\mu)N, \\ D_\mu \eta_i &= \left(\partial_\mu + i\frac{g}{2}\vec{\tau} \cdot \vec{W}_\mu + i\frac{g'}{2}\hat{B}_\mu + ig_X q_{\eta_i} \hat{Z}'_\mu\right)\eta_i, \end{aligned} \quad (2.12)$$

where $q_{N(\eta_i)}$ denotes the $U(1)_X$ charge of $N(\eta_i)$, and g and g' are the gauge couplings of $SU(2)_L$ and $U(1)_Y$, respectively. The NNZ' interaction can be immediately obtained as:

$$\mathcal{L}_{NNZ'} = -g_X q_N \bar{N} \gamma^\mu N \hat{Z}'_\mu. \quad (2.13)$$

Although the quartic gauge couplings of η_i to gauge bosons W^\pm , Z , γ , and \hat{Z}' can be derived from the kinetic terms of η_i , these couplings are irrelevant to our study here and are not presented explicitly. The various trilinear gauge couplings of η_i from $(D_\mu\eta_i)^\dagger(D^\mu\eta_i)$ can be summarized as:

$$\begin{aligned} \mathcal{L}_{\text{kin}} \supset & i\frac{g}{\sqrt{2}}\left\{\left[\partial_\mu\eta_i^-(S_i + iA_i) - \eta_i^-(\partial_\mu S_i + i\partial_\mu A_i)\right]W^{+\mu} + \text{H.c.}\right\} \\ & + \left(\frac{g}{2c_W}Z^\mu - g_X q_X \hat{Z}'^\mu\right)[(\partial_\mu S_i)A_i - S_i\partial_\mu A_i] \\ & + i\left(eA^\mu + \frac{1-2s_W^2}{2c_W}gZ^\mu + g_X q_X \hat{Z}'^\mu\right)[(\partial_\mu\eta_i^-)\eta_i^+ - \eta_i^-\partial_\mu\eta_i^+]. \end{aligned} \quad (2.14)$$

The W^\pm , Z , and γ gauge bosons and the Weinberg angle θ_W are defined through the relations:

$$\begin{aligned} W^\pm &= \frac{1}{\sqrt{2}}(W_\mu^1 \mp W_\mu^2), \\ A_\mu &= c_W \hat{B}_\mu + s_W W_\mu^3, \\ Z_\mu &= -s_W \hat{B}_\mu + c_W W_\mu^3, \end{aligned} \quad (2.15)$$

where c_W (s_W) $\equiv \cos \theta_W$ ($\sin \theta_W$) and $e = g s_W = g' c_W$ are used.

In the study of LFV processes, we need to know the photon and Z -boson gauge couplings to the SM particles. Therefore, the relevant photon and Z gauge couplings are given by:

$$\mathcal{L}_Z = -eQ_f \bar{f} \gamma_\mu f A^\mu - \frac{g}{2c_W} \bar{f} \left(C_R^f P_R + C_L^f P_L \right) \gamma_\mu f Z^\mu, \quad (2.16)$$

with

$$C_R^f = -2Q_f s_W^2, \quad C_L^f = 2T_f^3 - 2Q_f s_W^2, \quad (2.17)$$

where Q_f is the electric charge of the fermion f , and T_f^3 is its third component of the weak isospin.

3 Neutrino mass, lepton-flavor violation, kinetic mixing of gauge boson

Based on the introduced interactions, in this section we investigate the new physics effects on the rare lepton flavor related processes, such as neutrino mass, $\ell_i \rightarrow \ell_j \gamma$, $\ell_i \rightarrow 3\ell_j$, $\mu - e$ conversion in nuclei, and muonium-antimuonium oscillation. Note that throughout this section, we assume that the new physics effects dominate and ignore the SM contributions.

3.1 Scotogenic neutrino mass matrix

To obtain the Majorana neutrino mass in the model, we need both Yukawa couplings \mathbf{y}_1 and \mathbf{y}_2 , which can ensure that the structure of Majorana mass term $L^T C L$ can be achieved. In addition, since $\eta_{1,2}$ have no VEVs and the lepton number is preserved in the ground state, we are left with the choice of using the lepton number-violating interaction $\lambda_5 (H^\dagger \eta_1)(H^\dagger \eta_2)$ to generate the Weinberg's dimension-5 operator $LHHL$ [14]. For the purpose of clarity, we show a representative one-loop Feynman diagram in figure 1. According to the Yukawa couplings in eq. (2.10), the neutrino mass matrix elements can be obtained as:

$$m_{ij}^\nu = \frac{\sin(2\theta)}{16\pi^2} \bar{y}_{ij} m_N \left[\frac{m_{S_1}^2}{m_{S_1}^2 - m_N^2} \ln \left(\frac{m_{S_1}^2}{m_N^2} \right) - \frac{m_{S_2}^2}{m_{S_2}^2 - m_N^2} \ln \left(\frac{m_{S_2}^2}{m_N^2} \right) \right], \quad (3.1)$$

where we have included A_i contributions, $m_{A_i} = m_{S_i}$ is used, and the symmetric Yukawa couplings \bar{y}_{ij} in flavor indices are defined as:

$$\bar{y}_{ij} = y_{1i}^* y_{2j}^* + y_{2i}^* y_{1j}^*. \quad (3.2)$$

In the Ma model, the involved Yukawa couplings for m_{ij}^ν appear in the combination of $y_i y_j$; thus, the mass matrix elements have strong correlations. It needs at least two singlet right-handed fermions to explain the neutrino data. In our model, due to the introduction of one more inert Higgs doublet η_2 , the induced neutrino mass matrix elements appear in the combination of $y_{1i} y_{2j} + y_{2i} y_{1j}$ and have less correlations among the matrix elements. It is for this reason that the neutrino data can be accommodated using only one singlet fermion.

The symmetric mass matrix m^ν can be diagonalized through $m_{\text{dia}}^\nu = U^\dagger m^\nu U^*$, where $m_{\text{dia}}^\nu = \text{dia}(m_1, m_2, m_3)$ is the diagonal mass matrix. The unitary matrix U can be

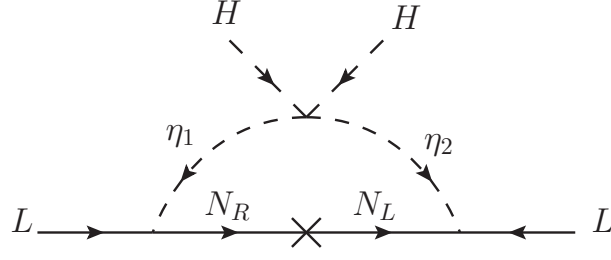


Figure 1. Sketched Feynman diagram mediated by Z_2 -odd particles for the radiative neutrino mass.

parametrized as:

$$U = \begin{pmatrix} c_{12}c_{13} & s_{12}c_{13} & s_{13}e^{-i\delta_{\text{CP}}} \\ -s_{12}c_{23} - c_{12}s_{13}s_{23}e^{i\delta_{\text{CP}}} & c_{12}c_{23} - s_{12}s_{13}s_{23}e^{i\delta_{\text{CP}}} & c_{13}s_{23} \\ s_{12}s_{23} - c_{12}s_{13}c_{23}e^{i\delta_{\text{CP}}} & -c_{12}s_{23} - s_{12}s_{13}c_{23}e^{i\delta_{\text{CP}}} & c_{13}c_{23} \end{pmatrix} \begin{pmatrix} e^{i\alpha_1} & & \\ & e^{i\alpha_2} & \\ & & 1 \end{pmatrix},$$

where c_{ij} (s_{ij}) $\equiv \cos \theta_{ij}$ ($\sin \theta_{ij}$), δ_{CP} is the Dirac CP-violating phase, and $\alpha_{1,2}$ are the Majorana phases. Consequently, the theoretical mass matrix obtained in eq. (3.1) can be determined by the observables from the neutrino oscillations, and their relations are given by:

$$\begin{aligned} (m^\nu)_{11} &= m_1 c_{12}^2 c_{13}^2 e^{i2\alpha_1} + m_2 s_{12}^2 c_{13}^2 e^{i2\alpha_2} + m_3 s_{13}^2 e^{-2i\delta_{\text{CP}}}, \\ (m^\nu)_{12} &= m_1 e^{2i\alpha_1} c_{12} c_{13} \left(-s_{12} c_{23} - e^{i\delta_{\text{CP}}} c_{12} s_{13} s_{23} \right) \\ &\quad + m_2 e^{2i\alpha_2} s_{12} c_{13} \left(c_{12} c_{23} - e^{i\delta_{\text{CP}}} s_{12} s_{13} s_{23} \right) + m_3 e^{-i\delta_{\text{CP}}} s_{13} c_{13} s_{23}, \\ (m^\nu)_{13} &= m_1 e^{2i\alpha_1} c_{12} c_{13} \left(s_{12} s_{23} - e^{i\delta_{\text{CP}}} c_{12} s_{13} s_{23} \right) \\ &\quad + m_2 e^{2i\alpha_2} s_{12} c_{13} \left(-c_{12} s_{23} - e^{i\delta_{\text{CP}}} s_{12} s_{13} c_{23} \right) + m_3 e^{-i\delta_{\text{CP}}} s_{13} c_{13} c_{23}, \\ (m^\nu)_{22} &= m_1 e^{2i\alpha_1} \left(-s_{12} c_{23} - e^{i\delta_{\text{CP}}} c_{12} s_{13} s_{23} \right)^2 \\ &\quad + m_2 e^{2i\alpha_2} \left(c_{12} c_{23} - e^{i\delta_{\text{CP}}} s_{12} s_{13} s_{23} \right)^2 + m_3 c_{13}^2 s_{23}^2, \\ (m^\nu)_{23} &= m_1 e^{2i\alpha_1} \left(s_{12} s_{23} - e^{i\delta_{\text{CP}}} c_{12} s_{13} c_{23} \right) \left(-s_{12} c_{23} - e^{i\delta_{\text{CP}}} c_{12} s_{13} s_{23} \right) \\ &\quad + m_2 e^{2i\alpha_2} \left(-c_{12} s_{23} - e^{i\delta_{\text{CP}}} s_{12} s_{13} c_{23} \right) \left(c_{12} c_{23} - e^{i\delta_{\text{CP}}} s_{12} s_{13} s_{23} \right) \\ &\quad + m_3 e^{-i\delta_{\text{CP}}} c_{13}^2 s_{23} c_{23}, \\ (m^\nu)_{33} &= m_1 e^{2i\alpha_1} \left(s_{12} s_{23} - e^{i\delta_{\text{CP}}} c_{12} s_{13} c_{23} \right)^2 \\ &\quad + m_2 e^{2i\alpha_2} \left(-c_{12} s_{23} - e^{i\delta_{\text{CP}}} s_{12} s_{13} c_{23} \right)^2 + m_3 c_{13}^2 c_{23}^2. \end{aligned} \tag{3.3}$$

3.2 Radiative lepton decay $\ell_i \rightarrow \ell_j \gamma$

Among the LFV processes, the most constraining process is the radiative muon decay $\mu \rightarrow e \gamma$. It can be the most important process to discover LFV due to the high sensitivity to the new physics effects. In order to study other radiative lepton decays, such as $\tau \rightarrow (e, \mu) \gamma$,

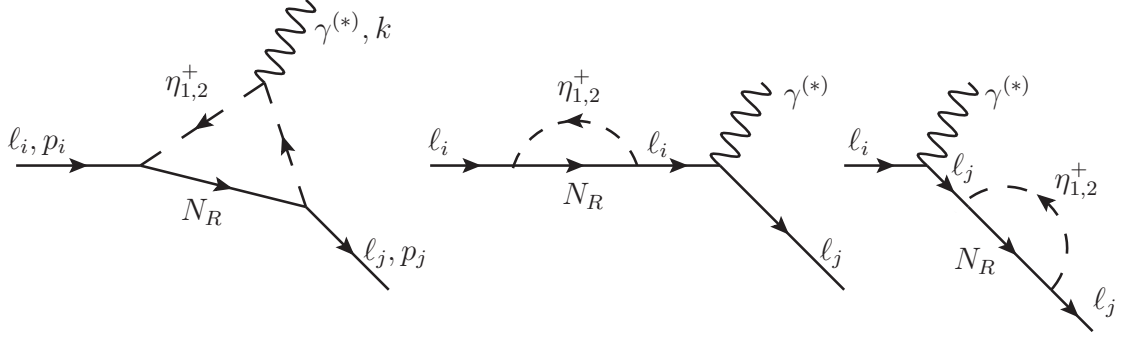


Figure 2. One-loop Feynman diagrams for $\ell_i \rightarrow \ell_j \gamma^{(*)}$.

in the following, we calculate the branching ratios for the $\ell_i \rightarrow \ell_j \gamma$ decays, where ℓ_j is the lighter lepton and its mass is neglected unless otherwise stated.

The radiative LFV process in the model arises from the η_i^\pm -mediated diagrams, as shown in figure 2. Using the Yukawa couplings in eq. (2.10), the loop-induced effective Lagrangian for $\ell_i \rightarrow \ell_j \gamma^{(*)}$ can be expressed as:

$$\mathcal{L}_{\ell_i \ell_j \gamma}^{\gamma} = ek^2 C_{1ji}^{\gamma} \bar{\ell}_j \gamma_{\mu} P_L \ell_i A^{\mu} - \frac{em_{\ell_i}}{2} C_{2ji}^{\gamma} \bar{\ell}_j \sigma_{\mu\nu} P_R \ell_i F^{\mu\nu}, \quad (3.4)$$

where the loop-induced Wilson coefficients are obtained as:

$$C_{1ji}^{\gamma} = \sum_{\alpha=1}^2 \frac{y_{\alpha i}^* y_{\alpha j}}{(4\pi)^2 m_{\eta_{\alpha}^{\pm}}^2} J_1^{\gamma} \left(\frac{m_N^2}{m_{\eta_{\alpha}^{\pm}}^2} \right), \quad (3.5)$$

$$C_{2ji}^{\gamma} = \sum_{\alpha=1}^2 \frac{y_{\alpha i}^* y_{\alpha j}}{(4\pi)^2 m_{\eta_{\alpha}^{\pm}}^2} J_2^{\gamma} \left(\frac{m_N^2}{m_{\eta_{\alpha}^{\pm}}^2} \right),$$

and the loop integral functions are defined by

$$J_1^{\gamma}(x) = \frac{1}{36(1-x)^4} (2 - 9x + 18x^2 - 11x^3 + 6x^3 \ln x), \quad (3.6)$$

$$J_2^{\gamma}(x) = \frac{1}{12(1-x)^4} (1 - 6x + 3x^2 + 2x^3 - 6x^2 \ln x).$$

The emitted photon can be on-shell ($k^2 = 0$) or off-shell ($k^2 \neq 0$), where the latter can be used to study the $\ell_i \rightarrow 3\ell_j$ process, in which a $\ell_j^+ \ell_j^-$ pair is produced by the off-shell photon. (The contribution of the Z -mediated diagrams is found to be small and will be neglected, as discussed in the next section.) Using the effective Lagrangian in eq. (3.4), the branching ratio for $\ell_i \rightarrow \ell_j \gamma$ can be obtained as [13]:

$$BR(\ell_i \rightarrow \ell_j \gamma) = \frac{3(4\pi)^3 \alpha_{\text{em}}}{4G_F^2} |C_{2ji}^{\gamma}|^2 BR(\ell_i \rightarrow \ell_j \bar{\nu}_j \nu_i), \quad (3.7)$$

with $\alpha_{\text{em}} = e^2/(4\pi)$.

In addition to the radiative LFV decays, the dipole operator in eq. (3.4) can contribute to the lepton anomalous magnetic dipole moment $(g - 2)$ when we replace ℓ_j by ℓ_i . As a result, the lepton $(g - 2)$ can be directly obtained as:

$$a_\ell \equiv \left(\frac{g - 2}{2} \right)_\ell = -m_\ell^2 C_{2\ell\ell}^\gamma. \quad (3.8)$$

3.3 $\ell_i \rightarrow 3\ell_j$ from penguin and box diagrams

We now discuss the three-body lepton flavor-changing decays. For simplicity, we only concentrate on the $\ell_i \rightarrow 3\ell_j$ decay. In the model, the LFV processes $\ell_i \rightarrow 3\ell_j$ can arise from photon-penguin, Z -penguin, and box diagrams. In the following, we discuss their contributions in sequence.

Since the effective interaction for $\ell_i \rightarrow \ell_j \gamma^*$ has been given in eq. (3.4), the transition amplitude with the assigned momenta for the $\ell_i(p) \rightarrow \ell_j(p_1) \ell^+(p_2) \ell^-(p_3)$ decay can be written as:

$$\begin{aligned} \mathcal{M}_\gamma = & e^2 C_{1ji}^\gamma \bar{u}(p_1) \gamma_\mu u(p) \bar{u}(p_3) \gamma^\mu v(p_2) \\ & + \frac{e^2 m_{\ell_i}}{k^2} C_{2ji}^\gamma \bar{u}(p_1) i \sigma_{\mu\nu} k^\nu u(p) \bar{u}(p_3) \gamma^\mu v(p_2) - (p_1 \leftrightarrow p_3), \end{aligned} \quad (3.9)$$

where the photon coupling to the SM charged lepton shown in eq. (2.16) is applied.

The Feynman diagrams for $\ell_i \rightarrow \ell_j Z^*$ are similar to the photon diagrams shown in figure 2, where we use Z^* instead of γ^* . Using the Z gauge couplings to η^\pm and the SM lepton, given in eqs. (2.14) and (2.16), the one-loop induced effective interaction for $\ell_i \ell_j Z$ can be obtained as:

$$\mathcal{L}_{\ell_i \ell_j Z}^Z = \frac{g c_{2W}}{c_W} \sum_{\alpha=1}^2 \frac{m_{\ell_i} m_{\ell_j}}{(4\pi)^2 m_{\eta_\alpha}^2} J_2^\gamma \left(\frac{m_N^2}{m_{\eta_\alpha}^2} \right) \bar{\ell}_j \gamma_\mu P_R \ell_i Z^\mu, \quad (3.10)$$

where we have dropped the small contributions from k^2 and k terms [13]. It can be clearly seen that the loop-induced Z coupling is proportional to the product of the lepton masses, i.e., $m_{\ell_i} m_{\ell_j}$. We note that because N does not couple to Z , the Z boson cannot be emitted from the fermion line in the loop; therefore, no chiral enhancement factor, e.g., $m_N^2/m_{\eta_i}^2$, appears in the model. When a necessary mass insertion occurs in the initial lepton ℓ_i , in order to balance the chirality of the lepton vector current that couples to the vector gauge boson Z , a mass factor is necessarily inserted in the final lepton ℓ_j . Hence, we get the result proportional to $m_{\ell_i} m_{\ell_j}$. Due to the fact that $m_{\ell_j} \ll m_{\ell_i}$ and $m_{\ell_i} m_{\ell_j}/m_Z^2 \ll 1$, we thus neglect the Z -penguin contributions to $\ell_i \rightarrow 3\ell_j$.

The box diagrams contributing to $\ell_i \rightarrow 3\ell_j$ are partly shown in figure 3. In addition to the diagrams mediated by the same $\eta_{1(2)}^\pm$, the other possible diagrams are mediated by both η_1^\pm and η_2^\pm and involve a chirality-flipping factor of m_N^2 . Using the Yukawa couplings in eq. (2.10), the four-fermion interaction for $\ell_i \rightarrow 3\ell_j$ is obtained as:

$$\mathcal{M}_{\text{box}} = (C_{1ji}^{\text{box}} + C_{2ji}^{\text{box}}) \bar{\ell}_j \gamma_\mu P_L \ell_j \bar{\ell}_j \gamma^\mu P_L \ell_i, \quad (3.11)$$

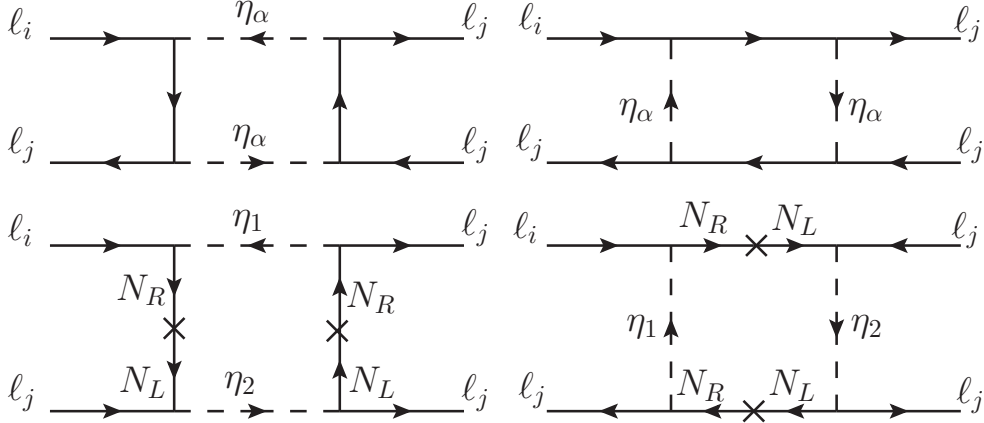


Figure 3. Selected box diagrams for $\ell_i \rightarrow 3\ell_j$.

where C_1^{box} denotes the contributions from diagrams involving the same $\eta_{1(2)}^\pm$ and C_2^{box} are from those involving both η_1^\pm and η_2^\pm , and the effective Wilson coefficients are given by:

$$C_{1ji}^{\text{box}} = - \sum_{\alpha=1}^2 \frac{y_{\alpha i}^* y_{\alpha j} |y_{\alpha j}|^2}{(4\pi)^2 m_{\eta_\alpha}^2} J_1^{\text{box}} \left(\frac{m_N^2}{m_{\eta_\alpha}^2} \right), \quad (3.12)$$

$$C_{2ji}^{\text{box}} = \frac{y_{1i}^* y_{1j} |y_{2j}|^2 + y_{2i}^* y_{2j} |y_{1j}|^2}{(4\pi)^2 m_{\eta_2}^2} \frac{m_N^2}{m_{\eta_2}^2} J_2^{\text{box}} \left(\frac{m_N^2}{m_{\eta_2}^2}, \frac{m_{\eta_1}^2}{m_{\eta_2}^2} \right),$$

with the loop integral functions given by

$$J_1^{\text{box}}(x) = \frac{1+x}{2(1-x)^2} + \frac{\ln x}{(1-x)^3}, \quad (3.13)$$

$$J_2^{\text{box}}(x, y) = -\frac{1}{(1-x)(y-x)} - \frac{(y-x^2) \ln x}{(1-x)^2(y-x)^2} + \frac{y \ln y}{(1-y)(y-x)^2}.$$

Although C_{2ji}^{box} seems to have a chiral enhancement, its contribution is in fact somewhat smaller than C_{1ji}^{box} due to the assumed condition that $m_N < m_{\eta_2}$.

Combining the contributions from the photon-penguin and box diagrams, the branching ratio for the $\ell_i \rightarrow 3\ell_j$ decay can be written as [13]:

$$BR(\ell_i \rightarrow 3\ell_j) = \frac{3(4\pi\alpha_{\text{em}})^2}{8G_F^2} \left[|C_{1ji}^\gamma|^2 + |C_{2ji}^\gamma|^2 \left(\frac{16}{3} \ln \left(\frac{m_i}{m_j} \right) - \frac{22}{3} \right) + \frac{|C_{ji}^{\text{box}}|^2}{6(4\pi\alpha_{\text{em}})^2} \right. \\ \left. + \frac{2}{3} \left(-6 \text{Re}(C_{1ji}^\gamma C_{2ji}^{\gamma*}) + \frac{1}{(4\pi\alpha_{\text{em}})^2} \text{Re} \left((C_{1ji}^\gamma - 2C_{2ji}^\gamma) C_{ji}^{\text{box}*} \right) \right) \right] \quad (3.14)$$

$$\times BR(\ell_i \rightarrow \ell_j \bar{\nu}_j \nu_i),$$

where $C_{ji}^{\text{box}} = C_{1ji}^{\text{box}} + C_{2ji}^{\text{box}}$.

3.4 $\mu - e$ conversion in nuclei and muonium-antimuonium oscillation

The $\mu - e$ conversion process describes the muon capture by a nucleus through the process $\mu(A, Z) \rightarrow e(A, Z)$. At the quark level, the process can be represented as $\mu q \rightarrow e q$, as induced by the photon- and Z -penguin diagrams in the model. Following the results in [16, 17], the conversion rate, which is relative to the muon capture rate, is given by:

$$CR(\mu - e, \text{Nucleus}) = \frac{p_e E_e m_\mu^3 G_F^2 \alpha_{\text{em}}^3 Z_{\text{eff}}^4 F_p^2}{8\pi^2 Z \Gamma_{\text{cap}}} \times \left[\left| A_+ \left(g_{LV}^{(0)} + g_{LS}^{(0)} \right) + A_- \left(g_{LV}^{(1)} + g_{LS}^{(1)} \right) \right|^2 + (R \leftrightarrow L) \right], \quad (3.15)$$

where p_e (E_e) is the momentum (energy) of electron and is taken to be m_μ in the numerical estimates, Z_{eff} denotes the effective atomic charge of the nucleus, F_p is the nuclear matrix element, Γ_{cap} is the total muon capture rate, $A_\pm = Z \pm \tilde{N}$ with Z (\tilde{N}) being the proton (neutron) number in the nucleus, and $g_{\chi K}^{(j)}$ with $\chi = L, R$ and $K = V, S$ are defined by

$$\begin{aligned} g_{\chi K}^{(0)} &= \frac{1}{2} \sum_{q=u,d,s} \left(g_{\chi K}^q G_K^{(q,p)} + g_{\chi K}^q G_K^{(q,n)} \right), \\ g_{\chi K}^{(1)} &= \frac{1}{2} \sum_{q=u,d,s} \left(g_{\chi K}^q G_K^{(q,p)} - g_{\chi K}^q G_K^{(q,n)} \right). \end{aligned} \quad (3.16)$$

Since the Z -penguin contribution is negligible, the dominant effect is from the photon-penguin diagrams. Thus, the only nonzero $g_{\chi K}^q$ is:

$$g_{LV}^q = \frac{\sqrt{2} e^2 Q_q}{G_F} (C_{1e\mu}^\gamma - C_{2e\mu}^\gamma). \quad (3.17)$$

The nucleon matrix element $G_K^{(q,N')}$ is defined by $\langle N' | \bar{q} \Gamma_K q | N' \rangle = G_K^{(q,N')} \bar{N}' \Gamma_K N'$, where $\Gamma_K = (1, \gamma_\mu)$ when $K = (S, V)$, respectively. Their values can be found in refs. [16, 18] as:

$$G_V^{(u,p)} = G_V^{(d,n)} = 2, \quad G_V^{(d,p)} = G_V^{(u,n)} = 1, \quad G^{(s,N')} = 0. \quad (3.18)$$

For heavy nuclei, because $A_- \ll A_+$ and $g_{\chi K}^{(1)} < g_{\chi K}^{(0)}$, the $\mu - e$ conversion rate in the model can be simplified as:

$$CR(\mu - e, \text{Nucleus}) \approx \frac{p_e E_e m_\mu^3 G_F^2 \alpha_{\text{em}}^3 Z_{\text{eff}}^4 F_p^2}{8\pi^2 Z \Gamma_{\text{cap}}} A_+^2 \left| g_{LV}^{(0)} \right|^2. \quad (3.19)$$

In addition to the $\mu - e$ conversion and LFV processes, which are $\Delta L_\mu = 1$ processes, another interesting process involving $\Delta L_\mu = 2$ ($\Delta L = 2$ will be used hereinafter) is the muonium-antimuonium oscillation, where the muonium is a bound state of μ^+ and e^- , i.e., $|M_\mu\rangle \equiv |\mu^+ e^-\rangle$. Similar to the $\mu \rightarrow 3e$ decay, the $M_\mu - \bar{M}_\mu$ mixing matrix element can arise from the box diagrams, where the Feynman diagrams are similar to figure 3 with $(\ell_i, \ell_j) = (\mu, e)$. As in the case of meson oscillations, $M_\mu - \bar{M}_\mu$ mixing effect can be taken as a perturbative effect in quantum mechanics and is formulated by [19]

$$\left(m - \frac{i}{2} \Gamma \right)_{12} = \frac{1}{2m_{M_\mu}} \langle \bar{M}_\mu | \mathcal{H}_{\text{eff}} | M_\mu \rangle + \frac{1}{m_{M_\mu}} \sum_n \frac{\langle \bar{M}_\mu | \mathcal{H}_{\text{eff}} | n \rangle \langle n | \mathcal{H}_{\text{eff}} | M_\mu \rangle}{m_{M_\mu} - E_n + i\epsilon}, \quad (3.20)$$

where m_{12} and Γ_{12} lead to the mass and lifetime differences between the two physical states of muonium, and n in the second term denotes the possible intermediate state. In order to produce the lifetime difference $\Delta\Gamma$, we need a resonant intermediate state. In the model, the new particle masses are heavier than the muonium mass m_{M_μ} . As such, $\Delta\Gamma$ by the new effects is negligible, and we concentrate on the mass difference $\Delta m = m_1 - m_2 \approx 2 \operatorname{Re}(m_{12})$. From eq. (3.20), the parameter $x \equiv \Delta m / \Gamma_\mu$ used to show the probability of $M_\mu \rightarrow \bar{M}_\mu$ can be written as:

$$x \approx \frac{1}{m_{M_\mu} \Gamma_\mu} \operatorname{Re}(\langle \bar{M}_\mu | \mathcal{H}_{\text{eff}} | M_\mu \rangle) . \quad (3.21)$$

Following the formulation obtained in ref. [19], the oscillation probability is:

$$P(M_\mu \rightarrow \bar{M}_\mu) = \frac{1}{2}(x^2 + y^2) \approx \frac{x^2}{2} , \quad (3.22)$$

while the experimental upper limit is:

$$P(M_\mu \rightarrow \bar{M}_\mu)^{\text{exp}} \leq 8.3 \times 10^{-11} / S_B(B_0) , \quad (3.23)$$

with $S_B(B_0) = 0.75$ [19, 20] taken in this work. Since the spin-0 para-muonium and spin-1 ortho-muonium are produced in the experiment [20], in order to compare the theoretical estimate with the experimental data, we follow the prescription given in ref. [19] and take the spin average by combining both spin-0 and spin-1 muonia as:

$$P(M_\mu \rightarrow \bar{M}_\mu)^{\text{exp}} = \sum_{i=P,V} \frac{1}{2s_i + 1} P(M_\mu^i \rightarrow \bar{M}_\mu^i) , \quad (3.24)$$

where s_i denotes the spin of the muonium M_μ^i .

According to the Yukawa couplings shown in eq. (2.10) and the Feynman diagrams in figure 3, the effective interaction for the $\Delta L = 2$ process can be written as:

$$\mathcal{H}_{\text{eff}} = C_1^{\Delta L=2} (\bar{\mu} \gamma_\mu P_L e) (\bar{\mu} \gamma^\mu P_L e) , \quad (3.25)$$

where the Wilson coefficient $C_1^{\Delta L=2}$ is given by:

$$C_1^{\Delta L=2} = \sum_{\alpha=1}^2 \frac{(y_{\alpha\mu} y_{\alpha e}^*)^2}{(4\pi)^2 m_{\eta_\alpha}^2} J_1^{\text{box}} \left(\frac{m_N^2}{m_{\eta_\alpha}^2} \right) - 2 \frac{y_{1\mu} y_{1e}^* y_{2\mu} y_{2e}^*}{(4\pi)^2 m_{\eta_2}^2} \frac{m_N^2}{m_{\eta_2}^2} J_2^{\text{box}} \left(\frac{m_N^2}{m_{\eta_2}^2}, \frac{m_{\eta_1}^2}{m_{\eta_2}^2} \right) . \quad (3.26)$$

Using the transition matrix element $\langle \bar{M}_\mu | O_1 | M_\mu \rangle = f_{M_\mu}^2 m_{M_\mu}^2$, the x -parameter for para-muonium and ortho-muonium are:

$$\begin{aligned} x_P &= \frac{4(m_{\text{red}} \alpha_{\text{em}})^3}{\pi \Gamma_\mu} C_1^{\Delta L=2} , \\ x_V &= -\frac{12(m_{\text{red}} \alpha_{\text{em}})^3}{\pi \Gamma_\mu} C_1^{\Delta L=2} , \end{aligned} \quad (3.27)$$

where the reduced mass $m_{\text{red}} = m_\mu m_e / (m_\mu + m_e)$, and $f_{M_\mu}^2 = 4(m_{\text{red}} \alpha_{\text{em}})^3 / m_{M_\mu}$ [19]. Hence, eq. (3.24) can be expressed as:

$$P(M_\mu \rightarrow \bar{M}_\mu)^{\text{exp}} = \frac{x_P^2}{2} + \frac{x_V^2}{6} . \quad (3.28)$$

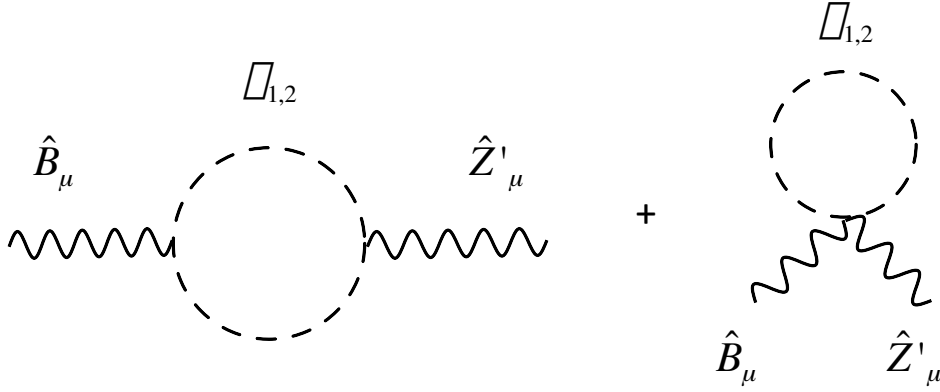


Figure 4. One-loop diagrams inducing kinetic mixing between $U(1)_Y$ and $U(1)_X$ gauge fields.

3.5 Loop-induced kinetic mixing between $U(1)_Y$ and $U(1)_X$

In our model, the SM particles do not interact with Z' boson at the tree level since they are not charged under $U(1)_X$. However, they interact with Z' through kinetic mixing between $U(1)_Y$ and $U(1)_X$ gauge fields induced by the one-loop diagrams shown in figure 4. We calculate these diagrams and obtain kinetic mixing term

$$\mathcal{L}_{KM} = -\frac{\sin \epsilon}{2} \hat{B}_{\mu\nu} \hat{Z}'^{\mu\nu}, \quad (3.29)$$

$$\begin{aligned} \sin \epsilon = & \frac{Q_X g_X g'}{2(4\pi^2)} \int_0^1 dx (1-x)(2x-1)^2 \\ & \times \left(\ln \left[\frac{x(1-x)q^2 - m_{\eta_2^\pm}^2}{x(1-x)q^2 - m_{\eta_1^\pm}^2} \right] + \ln \left[\frac{x(1-x)q^2 - m_{S_2}^2}{x(1-x)q^2 - m_{S_1}^2} \right] \right), \end{aligned} \quad (3.30)$$

where q^2 corresponds to the momentum carried by the gauge bosons. Note that the diagrams sum up to give a finite result for the kinetic mixing with divergences canceled between the contributions from the two inert doublet scalars carrying opposite charges under $U(1)_X$. For $q^2 \ll m_{\eta_{1,2}^\pm, S_{1,2}}^2$, we can approximate the formula of ϵ by

$$\sin \epsilon \sim \frac{Q_X g_X g'}{3(4\pi)^2} \left(\ln \frac{m_{\eta_2^\pm}}{m_{\eta_1^\pm}} + \ln \frac{m_{S_1}}{m_{S_2}} \right). \quad (3.31)$$

We can diagonalize the kinetic terms for \hat{Z}'_μ and B_μ via the following transformations [21]:

$$\begin{aligned} \hat{B}_\mu &= B_\mu - \tan \epsilon Z'_\mu, \\ \hat{Z}'_\mu &= \frac{1}{\cos \epsilon} Z'_\mu. \end{aligned} \quad (3.32)$$

where we approximate $\sin \epsilon \simeq \epsilon$ and $\cos \epsilon \simeq 1$ hereafter. After electroweak symmetry breaking, we obtain the mass terms for neutral gauge bosons as

$$\mathcal{L}_M = \frac{1}{2} m_Z^2 \tilde{Z}_\mu \tilde{Z}^\mu + m_Z^2 \epsilon_{SW} Z'_\mu \tilde{Z}^\mu + \frac{1}{2} m_{Z'}^2 Z'_\mu Z'^\mu, \quad (3.33)$$

where $m_Z = v\sqrt{g^2 + g'^2}/2$ and $\tilde{Z}_\mu = c_W W_\mu^3 - s_W B_\mu$. We then obtain mass eigenstates and eigenvalues of the neutral gauge bosons as

$$\{m_{Z_1}^2, m_{Z_2}^2\} = \frac{1}{2}(m_{Z'}^2 + m_Z^2) \mp \frac{1}{2}\sqrt{(m_{Z'}^2 - m_Z^2)^2 + 4\epsilon^2 s_W^2 m_Z^4},$$

$$\begin{pmatrix} Z_{1\mu} \\ Z_{2\mu} \end{pmatrix} = \begin{pmatrix} \cos\theta_{ZZ'} & -\sin\theta_{ZZ'} \\ \sin\theta_{ZZ'} & \cos\theta_{ZZ'} \end{pmatrix} \begin{pmatrix} \tilde{Z}_\mu \\ Z'_\mu \end{pmatrix}, \quad \tan 2\theta_{ZZ'} = \frac{2s_W\epsilon m_Z^2}{m_Z^2 - m_{Z'}^2}, \quad (3.34)$$

where we can approximate $m_{Z_1} \simeq m_Z$ and $m_{Z_2} \simeq m_{Z'}$ for tiny ϵ . The Z_1 and Z_2 bosons are to be identified as the physical massive gauge bosons and, to avoid the pedantry while being generally not confusing, will be referred to as the Z and Z' bosons. The Z' interaction with SM fermions f is now given by

$$\begin{aligned} \mathcal{L}_{Z'\bar{f}f} &= \sum_{\chi=L,R} \frac{g}{\cos\theta_W} Z'_\mu \bar{f}_\chi \gamma^\mu \left[S_{ZZ'}(T_3 - Q \sin^2\theta_W) + C_{ZZ'}\epsilon Y \sin\theta_W \right] f_\chi \\ &\equiv Z'_\mu \bar{f} \gamma^\mu (C_L^f P_L + C_R^f P_R) f, \end{aligned} \quad (3.35)$$

where T_3 is diagonal generator of $SU(2)_L$, Q is the electric charge operator, $S_{ZZ'} \equiv \sin\theta_{ZZ'}$, and $C_{ZZ'} \equiv \cos\theta_{ZZ'}$.

4 Numerical analysis

In this section, we perform numerical scans for the allowed parameter space and the corresponding ranges of various observables, which are then compared with current experimental bounds or the sensitivities that ongoing/future experiments can probe. We also calculate the DM relic density and check against the constraint of the direct search limit.

4.1 Inputs and constraints

From eq. (3.3), it can be seen that when the neutrino mixing angles and masses are determined, the parameters of $\mathbf{y}_{1,2}$, m_{S_i, A_i} , and m_N can be bounded. In order to get the allowed ranges for the free parameters, we take the values of the neutrino oscillation parameters obtained from the global fit in refs. [22, 23] as the inputs, where the global fit results with 3σ errors are given in table 2. Based upon the fit results, the ranges of the Majorana mass matrix elements in units of eV for the normal ordering (NO) and inverted ordering (IO) can be respectively estimated as:

$$\begin{aligned} \begin{pmatrix} |m_{11}^\nu| & |m_{12}^\nu| & |m_{13}^\nu| \\ |m_{21}^\nu| & |m_{22}^\nu| & |m_{23}^\nu| \\ |m_{31}^\nu| & |m_{32}^\nu| & |m_{33}^\nu| \end{pmatrix}_{\text{NO}} &\simeq \begin{pmatrix} 0.09 - 0.42 & 0.095 - 0.909 & 0.087 - 0.906 \\ 0.095 - 0.909 & 1.51 - 3.31 & 2.03 - 2.81 \\ 0.087 - 0.906 & 2.03 - 2.81 & 1.46 - 3.27 \end{pmatrix} \times 10^{-2}, \\ \begin{pmatrix} |m_{11}^\nu| & |m_{12}^\nu| & |m_{13}^\nu| \\ |m_{21}^\nu| & |m_{22}^\nu| & |m_{23}^\nu| \\ |m_{31}^\nu| & |m_{32}^\nu| & |m_{33}^\nu| \end{pmatrix}_{\text{IO}} &\simeq \begin{pmatrix} 1.50 - 4.97 & 0. - 3.81 & 0. - 3.88 \\ 0. - 3.81 & 0. - 3.05 & 0.65 - 2.60 \\ 0. - 3.88 & 0.65 - 2.60 & 0. - 3.16 \end{pmatrix} \times 10^{-2}, \end{aligned} \quad (4.1)$$

where $m_{1(3)} = 0$ for NO (IO) is applied. Since we do not have any information on the Majorana phases at the moment, we take $\alpha_{1,2} \in [-\pi, \pi]$. We then use eq. (4.1) to bound the free parameters.

	$\theta_{12}/^\circ$	$\theta_{13}/^\circ$	$\theta_{23}/^\circ$	$\delta_{\text{CP}}/^\circ$	$\Delta m_{21}^2 \times 10^5 [\text{eV}^2]$	$\Delta m_{3\ell}^2 \times 10^3 [\text{eV}^2]$
NO	(31.27, 35.87)	(8.25, 8.98)	(39.7, 50.9)	(144, 350)	(6.82, 8.04)	(2.43, 2.59)
IO	(31.27, 35.87)	(8.24, 9.02)	(39.8, 51.6)	(194, 345)	(6.82, 8.04)	(−2.574, −2.410)

Table 2. Global fit with 3σ ranges based upon the observations of neutrino oscillations [22, 23].

	$\mu \rightarrow e\gamma$	$\mu \rightarrow 3e$	$\tau \rightarrow e\gamma$	$\tau \rightarrow \mu\gamma$	$\tau \rightarrow 3e$	$\tau \rightarrow 3\mu$	$CR(\mu - e, \text{Ti})$
U.L.	4.2×10^{-13}	1.0×10^{-12}	3.3×10^{-8}	4.4×10^{-8}	2.7×10^{-8}	2.1×10^{-8}	4.3×10^{-12} [24]

Table 3. Current upper bounds on various LFV processes. Except for the $\mu - e$ conversion rate in titanium quoted from ref. [24], all other values are obtained from the Particle Data Group [25].

The parameter space can be further constrained by various LFV processes, whose current upper bounds are given in table 3. With $S_B(B_0) = 0.75$, the upper limit on the probability of the muonium oscillation is taken as $P(M_\mu \rightarrow \bar{M}_\mu)^{\text{exp}} < 11.1 \times 10^{-11}$ [19, 20].

There are 12 free parameters involved in the model, and we only have 6 observables from the neutrino oscillation experiments. In order to make the parameter scans more efficient, following the strict constraint from the $\mu \rightarrow e\gamma$ decay shown in eqs. (3.5) and (3.7), we assume

$$y_{2\mu} = -\frac{m_{S_2}^2 y_{1e}^*}{m_{S_1}^2 y_{2e}^*} \frac{J_2^\gamma\left(\frac{m_N^2}{m_{S_1}^2}\right)}{J_2^\gamma\left(\frac{m_N^2}{m_{S_2}^2}\right)} + \xi e^{i\phi}, \quad (4.2)$$

where ξ is a real parameter and ϕ is its phase. The parameter ranges used to scan the parameter space are taken as follows:

$$\begin{aligned} m_N &\in [100, 1000] \text{ GeV}, & m_{S_{1,2}} &\in [800, 2500] \text{ GeV}, \\ y_{1i, 2i \neq \mu} &\in [-1, 1], & \phi_{1,3} &\in [-\pi, \pi], & \xi &\in [-0.1, 0.1], & \phi &\in [-\pi, \pi]. \end{aligned} \quad (4.3)$$

In addition, we also assume $m_N < m_{S_1} < m_{S_2}$ and $m_{\eta_i^\pm} = m_{S_i}$ in the numerical estimates.

Under the constraints of table 2 and table 3, we have sampled 10^9 points with the ranges of involved parameters shown in figure 5, where the black (red) points denote the NO (IO) neutrino mass. Figures 5(a)–(c) show the allowed ranges of various products of Yukawa couplings in absolute values that will appear in the calculations of LFV processes, while figure 5(d) shows those of m_{N, S_1} . The plots indicate that the constrained Yukawa couplings in the model are not sensitive to the neutrino mass ordering.

4.2 Correlations among the LFV processes

In this subsection, we numerically discuss the influence of parameters on the rare LFV processes and the correlations among the considered LFV processes in detail. Since the $\mu \rightarrow e\gamma$ decay is the most constraining LFV process at present and in foreseeable future, we first show its branching ratio dependence on the parameters and then investigate various correlations among the LFV processes.

According to eq. (3.7), the branching ratio for $\mu \rightarrow e\gamma$ can be taken as a function of $|y_{ie} y_{i\mu}^*|/m_{\eta_i^\pm}^2$. Based upon the scanning results exhibited in figure 5, we show the scatter

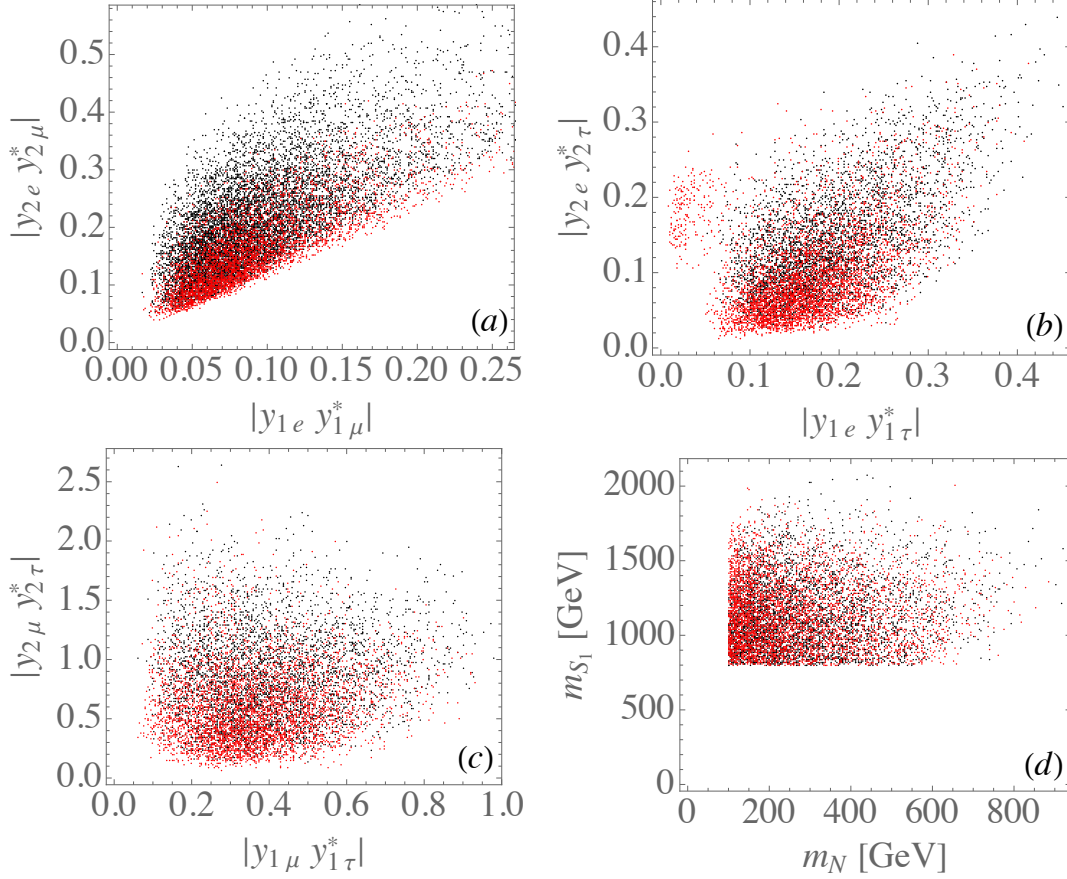


Figure 5. (a)–(c) Constraints on various products of Yukawa couplings, and (d) allowed ranges of m_{N,S_1} . The black and red points denote the results of NO and IO, respectively.

plots for $BR(\mu \rightarrow e\gamma)$ as a function of $|y_{1e}y_{1\mu}^*|/m_{\eta_i^\pm}^2$ and $|y_{2e}y_{2\mu}^*|/m_{\eta_i^\pm}^2$ in figure 6(a) and (b), respectively, where the horizontal dashed line denotes the sensitivity of MEG II experiment [3]. Since the MEG II experiment can only probe $\mu \rightarrow e\gamma$ down to the level of 6×10^{-14} , we have further restricted the model parameters to satisfy $BR(\mu \rightarrow e\gamma) \in (0.05, 5) \times 10^{-13}$ in the plots. As shown in the plots, the difference between the dependence on $|y_{1e}y_{1\mu}^*|/m_{\eta_1^\pm}^2$ and that on $|y_{2e}y_{2\mu}^*|/m_{\eta_2^\pm}^2$ is insignificant. As given in eqs. (3.15) and (3.17), the $\mu - e$ conversion rate arises from the photon-penguin diagram in the model. Thus, we show $CR(\mu - e, \text{Ti})$ as a function of $|y_{1e}y_{1\mu}^*|/m_{\eta_1^\pm}^2$ in figure 6(c), where the dashed line is the sensitivity of COMET [5] and Mu2e [6] experiments. As such, these experiments have the capability to probe most of the considered parameter space through the $\mu - e$ conversion rate. The correlation between $BR(\mu \rightarrow e\gamma)$ and $CR(\mu \rightarrow e, \text{Ti})$ is plotted in figure 6(d). Again, when the measurement of $CR(\mu - e, \text{Ti}) \sim 10^{-18}$ achieves the expected sensitivity, the parameter space with $BR(\mu \rightarrow e\gamma) \gtrsim O(10^{-13})$ is mostly covered. Hence, the $\mu - e$ conversion process has the potential to become the most stringent constraint among the LFV processes.

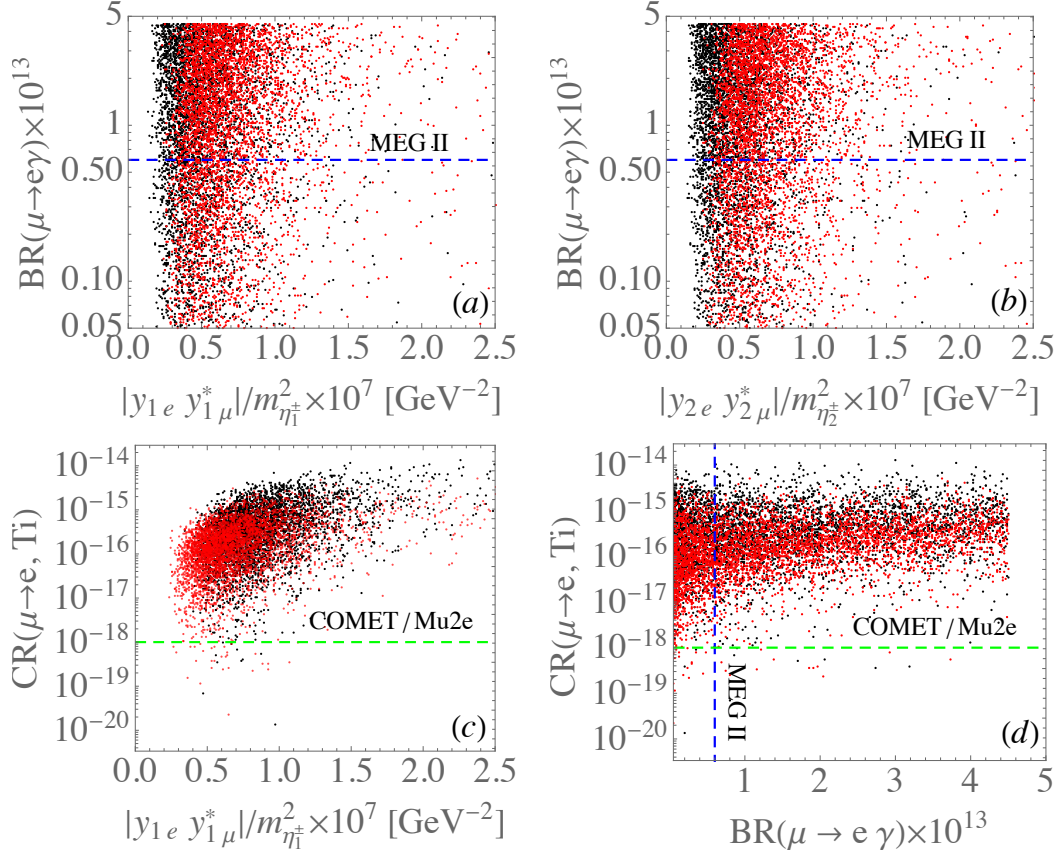


Figure 6. (a) and (b) $BR(\mu \rightarrow e\gamma)$ (in units of 10^{-13}) as a function of $|y_{ie}y_{i\mu}^*|/m_{\eta_i^{\pm}}^2$; (c) $\mu - e$ conversion rate as a function of $|y_{1e}y_{1\mu}^*|/m_{\eta_1^{\pm}}^2$; and (d) correlation between $BR(\mu \rightarrow e\gamma)$ and $CR(\mu - e, \text{Ti})$, where the dashed lines are the sensitivities of currently ongoing experiments. The black and red points denote the results of NO and IO, respectively.

As stated earlier, in addition to the photon-penguin diagrams, the $\mu \rightarrow 3e$ decay can be induced by the box diagrams in the model. To exhibit the role of the box diagrams, the ratio of $BR(\mu \rightarrow 3e)$ purely from the photon-penguin contribution to $BR(\mu \rightarrow e\gamma)$ can be expressed as:

$$R_{3e/e\gamma} = \frac{BR(\mu \rightarrow 3e)_{\gamma}}{BR(\mu \rightarrow e\gamma)} \approx \frac{\alpha_{\text{em}}}{8\pi} \left[\frac{|C_{1e\mu}^{\gamma}|^2}{|C_{2e\mu}^{\gamma}|^2} + \frac{16}{3} \ln \frac{m_{\mu}}{m_e} - \frac{22}{3} - 4 \text{Re} \left(\frac{C_{1e\mu}^{\gamma}}{C_{2e\mu}^{\gamma}} \right) \right]. \quad (4.4)$$

With $C_{1e\mu}^{\gamma}/C_{2e\mu}^{\gamma} \sim \mathcal{O}(1)$, the ratio in eq. (4.4) can be estimated to be $R_{3e/e\gamma} \sim 5 \times 10^{-3}$. Using the constrained parameter values shown in figure 5, indeed, we approximately obtain $R_{3e/e\gamma} \in (0.5, 5) \times 10^{-2}$. We can conclude that if $BR(\mu \rightarrow 3e) > BR(\mu \rightarrow e\gamma)$ is observed in experiments, the enhancement should arise from other effects than from the photon-penguin diagrams.

If we assume that the photon-penguin contribution to $\mu \rightarrow 3e$ is subleading, it is interesting to compare the $\mu \rightarrow 3e$ decay with the muonium oscillation, where both processes are dominated by the box diagrams. Implementing the constrained parameter values

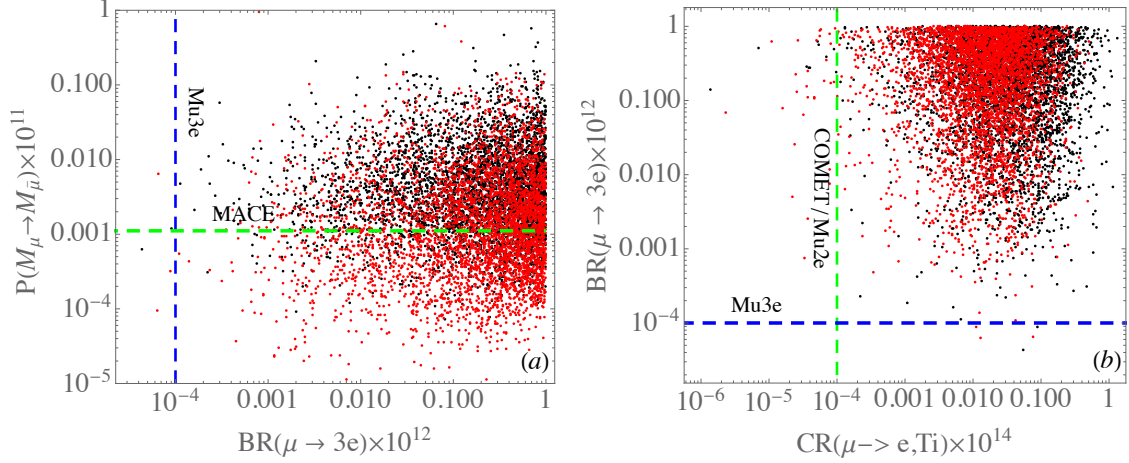


Figure 7. Correlation between $BR(\mu \rightarrow 3e)$ and (a) $P(M_\mu - \bar{M}_\mu)$ and (b) $CR(\mu - e, \text{Ti})$, where the dashed lines label the experimental sensitivities. The black and red points denote the results of NO and IO, respectively.

shown in figure 5 to the formulas in eqs. (3.14) and (3.28), we plot the correlation between $P(M_\mu - \bar{M}_\mu)$ and $BR(\mu \rightarrow 3e)$ in figure 7(a), where the dashed lines label the sensitivities of Mu3e and MACE experiments. It is seen that the predicted values of $P(M_\mu - \bar{M}_\mu)$ in the model are mostly below the current experimental limit of 4.3×10^{-12} when the $\mu \rightarrow 3e$ decay is constrained to satisfy the current upper limit of 1.0×10^{-12} . However, when $BR(\mu \rightarrow 3e)$ reaches the sensitivity of 10^{-16} , the decay can cover most of the considered parameter space, i.e., under the presumption that $BR(\mu \rightarrow e\gamma) \in (0.05, 5)10^{-13}$. We thus see that the two strictest constraints on the $\mu \rightarrow e$ transitions come from the $\mu - e$ conversion in nuclei and the $\mu \rightarrow 3e$ decay. Their correlation in the model can be found in figure 7(b). As such, if we do not see any evidence of the model in the LFV experiments, the highly sensitive measurements of $BR(\mu \rightarrow 3e)$ and $\mu - e$ conversion rate severely constrain the $\mu \rightarrow e\gamma$ decay and munoium oscillation processes.

After discussing the rare $\mu \rightarrow e$ transition, we discuss in the following analysis the lepton flavor-changing effects on the heavy τ -lepton decays, where the sensitivities assuming 50 ab^{-1} of data at Belle II can reach [11]:

$$\begin{aligned} BR(\tau \rightarrow \ell\gamma) &\sim 10^{-8} - 10^{-9}, \\ BR(\tau \rightarrow 3\ell) &\sim 10^{-9} - 10^{-10}, \end{aligned} \quad (4.5)$$

with $\ell = e, \mu$. Analogous to $\mu \rightarrow e\gamma$, the radiative τ decay also arises from the same types of diagrams. Therefore, using eq. (3.7) and the constrained parameter values, we plot the correlation between $BR(\tau \rightarrow e\gamma)$ and $BR(\mu \rightarrow e\gamma)$ in figure 8(a), where the dashed lines are the sensitivities of MEG II and Belle II experiments. Since the resulting branching ratio for $\tau \rightarrow e\gamma$ is lower than the sensitivity of Belle II, it is difficult to observe the $\tau \rightarrow e\gamma$ decay in the model. In figure 8(b), we show the correlation between $BR(\tau \rightarrow \mu\gamma)$ and $BR(\tau \rightarrow e\gamma)$. It can be found that unlike the $\tau \rightarrow e\gamma$ decay, the branching ratio for $\tau \rightarrow \mu\gamma$ can be as large as $O(10^{-8})$. As such, $\tau \rightarrow \mu\gamma$ serves as a good candidate to probe the new physics effects of the model in Belle II experiment.

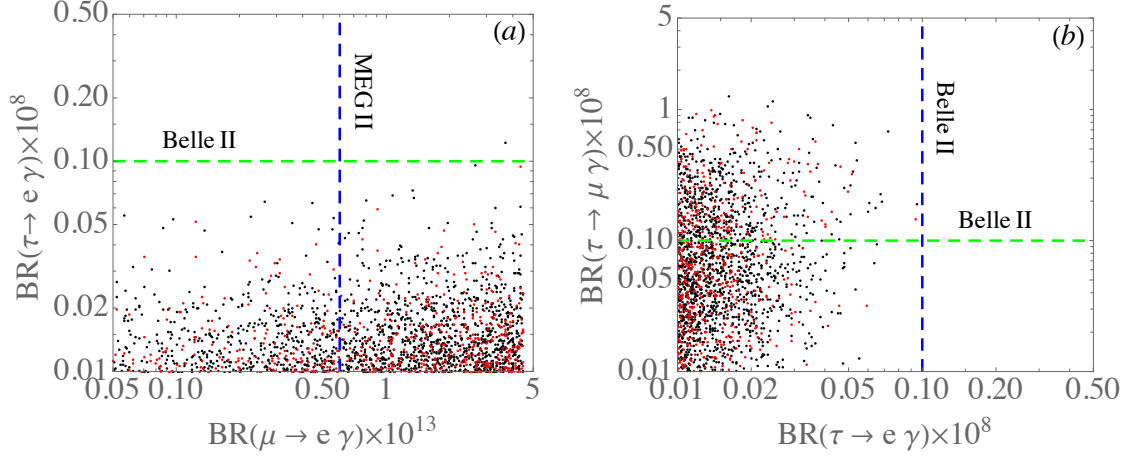


Figure 8. Correlation of BR in LFV processes: (a) $\tau \rightarrow e\gamma$ and $\mu \rightarrow e\gamma$, and (b) $\tau \rightarrow \mu\gamma$ and $\tau \rightarrow e\gamma$. The black and red points denote the results of NO and IO, respectively.

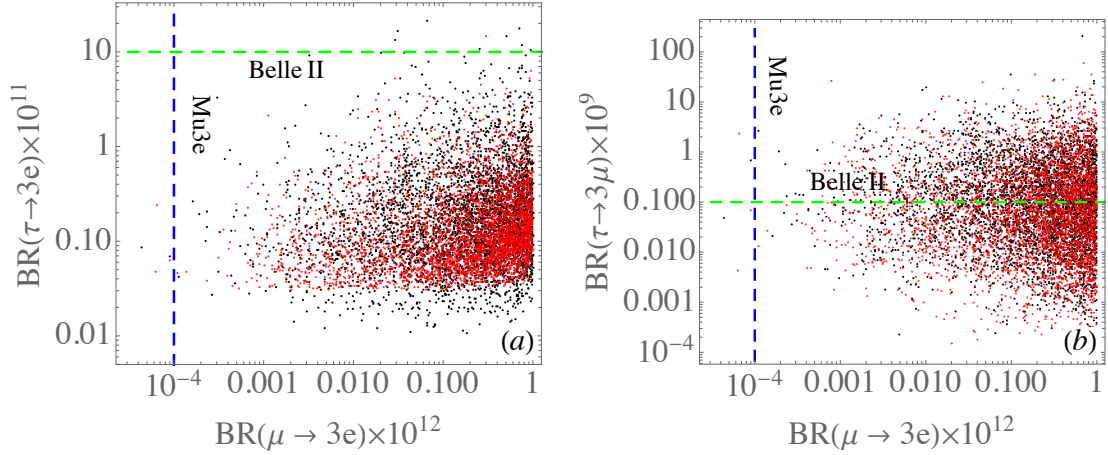


Figure 9. Correlation of BR between $\mu \rightarrow 3e$ and (a) $\tau \rightarrow 3e$ and (b) $\tau \rightarrow 3\mu$. The black and red points denote the results of NO and IO, respectively.

As discussed earlier, although the $\ell_i \rightarrow 3\ell_j$ decay is induced by the photon-penguin and box diagrams, the effects of the latter are more dominant. In order to reveal their contributions to $\tau \rightarrow 3e$ and $\tau \rightarrow 3\mu$, we show their branching ratio correlations with $\mu \rightarrow 3e$ in figure 9. Similar to $\tau \rightarrow e\gamma$, it is difficult for Belle II to reach the predicted $BR(\tau \rightarrow 3e)$ in the model. Nevertheless, the $\tau \rightarrow 3\mu$ decay is more promising to detect at Belle II because the value can reach $O(10^{-9} - 10^{-10})$.

We finally make some remarks on the lepton $(g-2)$'s shown in eq. (3.8). It is known that the lepton $(g-2)$ mediated by the charged scalar boson is usually negative. Although the sign of a_μ in the model contradicts with that given by the recent E989 experiment at Fermilab [26], its value $|a_\mu| < 10^{-11}$ due to the m_μ^2 dependence and $m_{\eta^\pm} \sim O(1)$ TeV. Therefore, if the muon $g-2$ anomaly can be resolved within the SM [27], the negative a_μ of the model will not cause a serious problem. On the other hand, the electron $(g-2)$ in the model can be estimated as $|a_e| < 10^{-17}$ and is negligible.

4.3 DM relic density and DM-nucleon scattering cross section

In this subsection, we discuss the DM phenomenology in our model. Our DM candidate is the vector-like neutral fermion N which interacts with the SM particles via the Yukawa couplings in eq. (2.9) and the Z' exchange with the kinetic mixing effect. In the estimate of relic density, the dominant DM annihilation processes are summarized as follows:

- $N\bar{N} \rightarrow Z' \rightarrow f_{SM}\bar{f}_{SM}, W^+W^-$.
- $N\bar{N} \rightarrow Z'Z'$.
- $\{N\bar{N}, NN, \bar{N}\bar{N}\} \rightarrow \{\nu\bar{\nu}, \nu\nu, \bar{\nu}\bar{\nu}, \ell^+\ell^-\}$,

where ℓ^\pm and f_{SM} denote the SM charged leptons and fermions, respectively. The first two processes are mediated by the new gauge interactions, while the last channels rely mostly on the new Yukawa couplings. We estimate the relic density of DM using `micrOMEGAs` 5.2.4 [28] implemented with the new interaction vertices in the model.

We first discuss the relic density by considering only Z' interactions and choosing vanishing Yukawa couplings for the DM mass in the range of 100 GeV to 1 TeV. For illustration purposes, we consider two specific cases; (1) $m_N = 2m_{Z'}$ where the $N\bar{N} \rightarrow Z'Z'$ process is dominant, (2) $m_{Z'} = 2.025m_N$ where the $N\bar{N} \rightarrow Z' \rightarrow \{f_{SM}\bar{f}_{SM}, W^+W^-\}$ processes are dominant. The relic density is then estimated by scanning the values of $\{m_N, g_X\}$. The left and right plots in figure 10 show the parameter regions in the m_N - g_X plane that give the relic density $0.11 < \Omega h^2 < 0.13$ [25] for cases (1) and (2), respectively. For case (1), the gauge coupling around $0.2 \lesssim g_X \lesssim 0.7$ can accommodate the observed relic density in the assumed DM mass range. For case (2), on the other hand, a larger gauge coupling is required and the observed relic density can be explained only when $m_N \lesssim 400$ GeV imposing perturbative condition $g_X < \sqrt{4\pi}$. This behavior is due to the fact that the small kinetic mixing for the s -channel annihilation via Z' exchange is suppressed.

Secondly, we discuss the relic density by use of the Yukawa couplings that satisfy the neutrino oscillation observations and flavor-changing constraints given in the previous subsections. For illustration purposes, we consider a vanishing gauge coupling g_X and focus on the effects of Yukawa couplings. Figure 11 shows the DM relic density as a function of m_N where the black and red points correspond to allowed parameter sets in the NO and IO scenarios, respectively. We find that the observed relic density can be explained by the Yukawa interactions for $m_N \lesssim 650$ GeV and that it gets smaller than the observed value in the heavier DM region. This is because the Yukawa couplings get larger in the heavier mass region, as required to fit the neutrino oscillation data. We note in passing that it is possible to utilize the Z' interactions to shift the scatter points downwards by turning on the gauge coupling g_X and tuning its value and the Z' mass.

Thirdly, we comment on the constraint from indirect detection of DM. DM annihilation cross section in the current Universe is constrained by indirect detection for which Fermi-LAT gamma-ray observation [29, 30] provides the strongest limit of $\mathcal{O}(100)$ GeV on the DM mass when DM pair annihilates into final states containing charged particles. For $m_{DM} \gtrsim 100$ GeV, the upper limit of thermally averaged DM annihilation cross section is

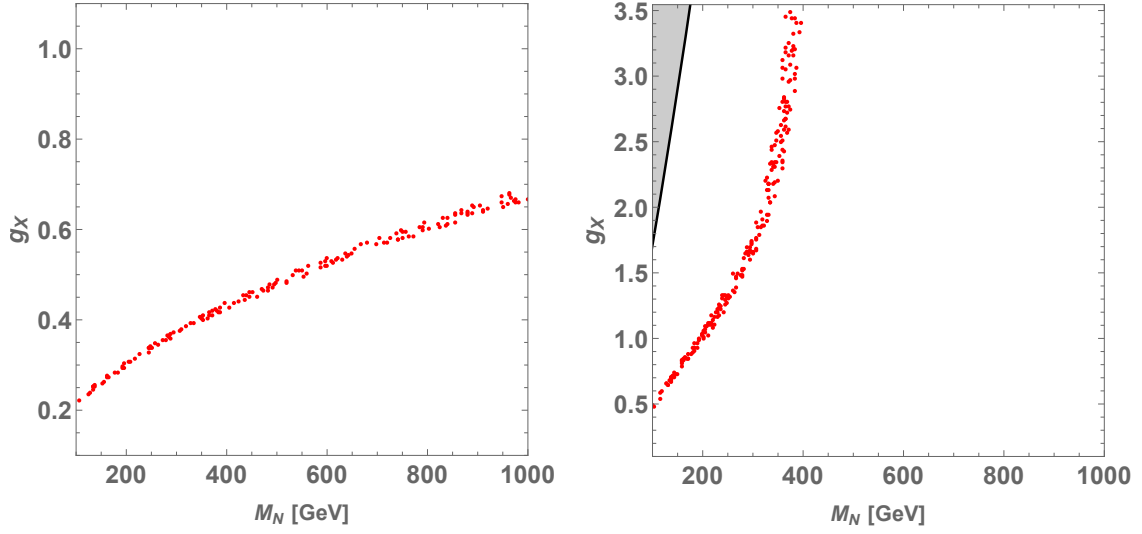


Figure 10. Scatter plots of the parameter region in the m_N - g_X plane that satisfies $0.11 < \Omega h^2 < 0.13$, considering only the Z' interactions. The left and the right plots correspond to cases of $m_N = 2m_{Z'}$ and $m_{Z'} = 2.025m_N$, respectively. The gray region is excluded by XENON1T.

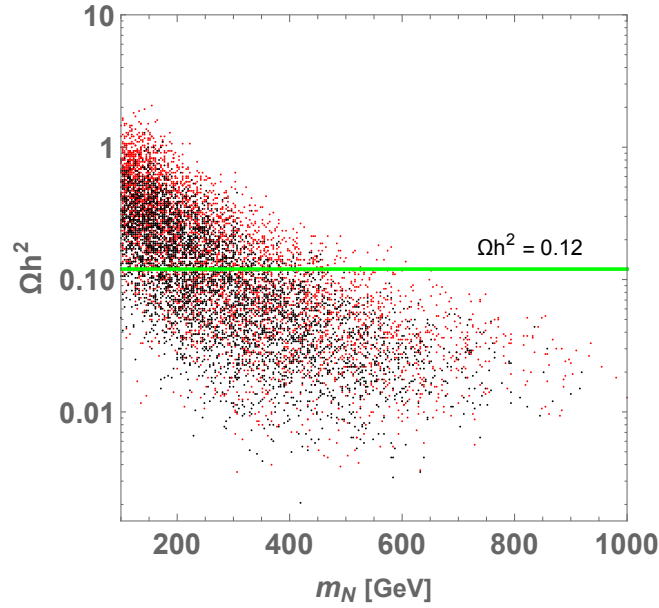


Figure 11. Scatter plot of the relic density of N for the allowed parameter sets with $g_X \rightarrow 0$. The black and red points denote the results of NO and IO, respectively.

larger than the value that explains the observed relic density, $\langle \sigma v \rangle \sim 3 \times 10^{-26} \text{ cm}^3 \text{ s}^{-1}$ during the freeze-out period, where the upper limit is larger for the heavier mass regime. In our scenarios, DM annihilation cross sections in the current Universe satisfy the indirect detection constraint. More explicitly, we obtain $\langle \sigma v \rangle \sim 3 \times 10^{-26} \text{ cm}^3 \text{ s}^{-1}$ for the $N\bar{N} \rightarrow Z'Z'$ mode, and $\langle \sigma v \rangle < 3 \times 10^{-26} \text{ cm}^3 \text{ s}^{-1}$ for the $N\bar{N} \rightarrow Z' \rightarrow \bar{f}f$ mode with $2m_{DM} \lesssim m_{Z'}$ and the $N\bar{N} \rightarrow \bar{\ell}\ell(\bar{\nu}\nu)$ mode via Yukawa interaction.

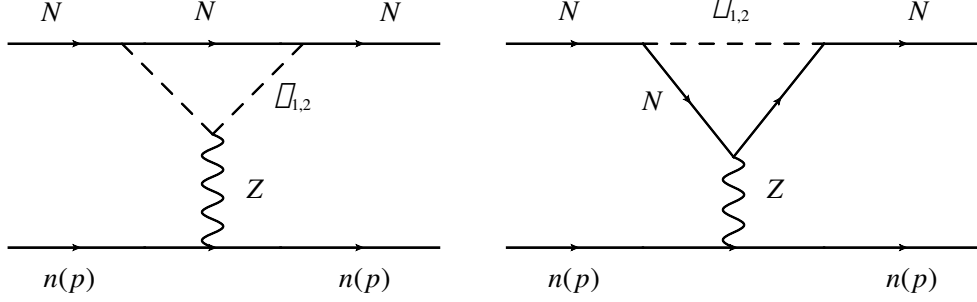


Figure 12. One-loop diagrams inducing DM-nucleon scattering.

Finally, we discuss the DM-nucleon scattering cross section. The effective interactions between DM and nucleon arising from the $Z' - Z$ mixing can be expressed as:

$$\begin{aligned} \mathcal{L}_{\text{eff}}^{Z'} &= \frac{g_X}{m_{Z'}^2} C_{nnZ'} (\bar{N} \gamma^\mu N) (n \gamma_\mu n) + \frac{g_X}{m_{Z'}^2} C_{ppZ'} (\bar{N} \gamma^\mu N) (p \gamma_\mu p), \\ C_{nnZ'} &= \sum_{\chi=L,R} (C_\chi^u + 2C_\chi^d), \quad C_{ppZ'} = \sum_{\chi=L,R} (2C_\chi^u + C_\chi^d), \end{aligned} \quad (4.6)$$

where n (p) stands for the neutron (proton), $\mu_{n(p)} \equiv m_N m_{n(p)} / (m_N + m_{n(p)})$, and $C_{L(R)}^f$ is given in eq. (3.35). In addition, the loop-induced NNZ coupling from the Yukawa couplings can be obtained from figure 12 as:

$$\begin{aligned} \mathcal{L}_{\text{eff}}^Z &= -\frac{g}{2c_W} \frac{C_{NNZ}}{m_Z^2} (\bar{N} \gamma^\mu N) (n \gamma_\mu n) - \frac{g}{c_W} \left(\frac{1}{2} - 2s_W^2 \right) \frac{C_{NNZ}}{m_Z^2} (\bar{N} \gamma^\mu N) (p \gamma_\mu p), \\ C_{NNZ} &= \sum_{a=1}^2 \sum_{i=1}^3 (-1)^a \frac{g s_W^2 y_{ai} y_{ai}^*}{(4\pi)^2 c_W} \int_0^1 dx \int_0^{1-x} dy \left[\frac{m_N^2 (1-x)(1-y)}{\Delta(m_N^2, m_{S_a}^2)} + \ln \frac{\tilde{\Delta}(m_N^2, m_{S_a}^2)}{\Delta(m_N^2, m_{S_a}^2)} \right], \\ \Delta(m_N^2, m_{S_a}^2) &= -[x(1-x) + y(1-y) + 2xy]m_N^2 + m_{S_a}^2(1-x-y), \\ \tilde{\Delta}(m_N^2, m_{S_a}^2) &= -[x(1-x) + y(1-y) + 2xy]m_N^2 + m_{S_a}^2(x+y). \end{aligned} \quad (4.7)$$

Accordingly, the spin-independent (SI) DM-nucleon scattering cross section in the non-relativistic limit can be written as [31]:

$$\begin{aligned} \sigma_{SI} &\sim \frac{\mu_n^2}{2\pi} \left[\frac{A-Z}{A} \left(\frac{g_X}{m_{Z'}^2} C_{nnZ'} - \frac{g}{2c_W} \frac{C_{NNZ}}{m_Z^2} \right) \right. \\ &\quad \left. + \frac{A}{Z} \left(\frac{g_X}{m_{Z'}^2} C_{ppZ'} - \frac{g}{2c_W} (1-4s_W^2) \frac{C_{NNZ}}{m_Z^2} \right) \right]^2, \end{aligned} \quad (4.8)$$

where Z and A are the atomic number and the atomic mass of the target nucleus, respectively. It is found that the scattering cross section tends to be dominated by the effective interactions in eq. (4.7) for $m_{Z'} > m_Z$ and/or small g_X . In figure 13, we show the scattering cross section for the xenon target ($A = 131$, $Z = 54$) as a function of DM mass for small g_X , where we choose $m_{S_1} = m_{S_2} = 1500$ GeV and $\sum_{ai} (-1)^a y_{ai} y_{ai}^* = 0.03$ and 0.05 for illustration purposes. As shown, the cross sections are mostly below the gray region excluded by XENON1T [10]. Thus, the constraint from DM direct detection can

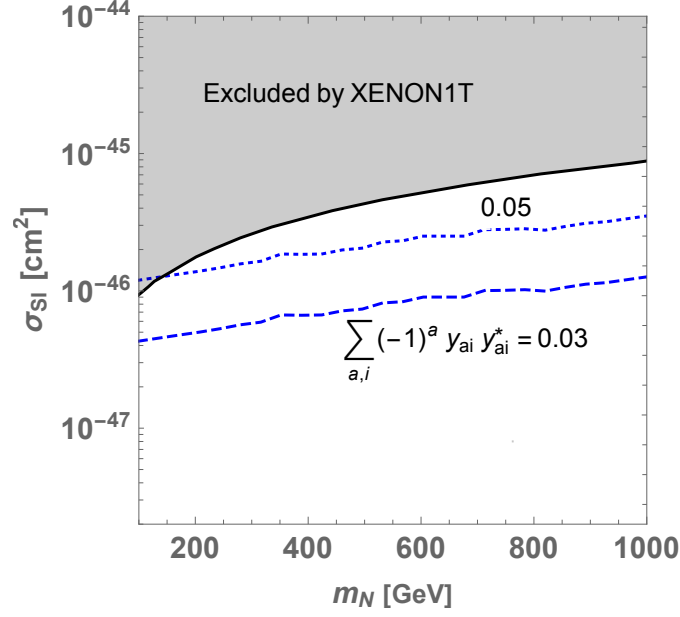


Figure 13. DM-neutron scattering cross section as a function of m_N , for $\sum_{a,i} (-1)^a y_{ai} y_{ai}^* = 0.03$ and 0.05 along with $m_{S_1} = m_{S_2} = 1500$ GeV. The gray region is excluded by XENON1T.

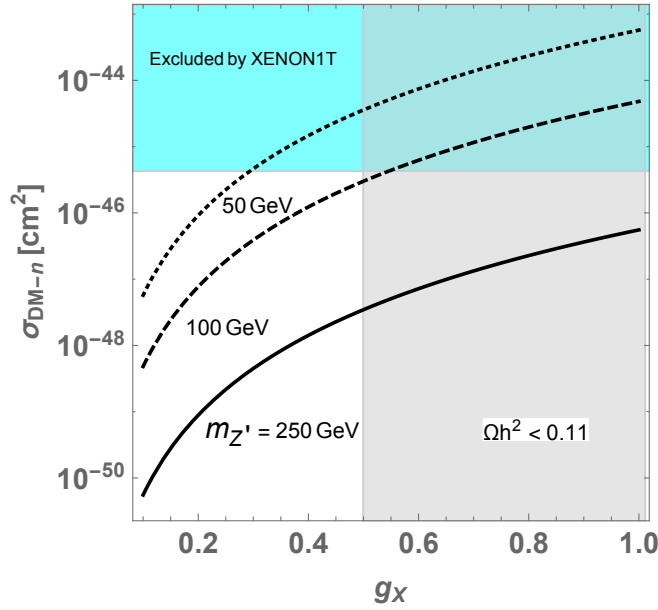


Figure 14. DM-neutron scattering cross section as a function of g_X for $m_{Z'} = 50, 100$, and 250 GeV. The gray region is excluded by $\Omega h^2 \lesssim 0.11$ and the light blue region is excluded by XENON1T, assuming $m_N = 500$ GeV.

be avoided if $|\sum_{ai} (-1)^a y_{ai} y_{ai}^*| \lesssim 0.05$, where the condition can be easily achieved in the model. When the contributions from the loop-induced NNZ coupling is suppressed, the σ_{SI} as a function of g_X for $m_{Z'} = 50, 100$, and 250 GeV along with $m_N = 500$ GeV is shown in figure 14. The gray region has $\Omega h^2 \lesssim 0.11$ and the cyan region is excluded by

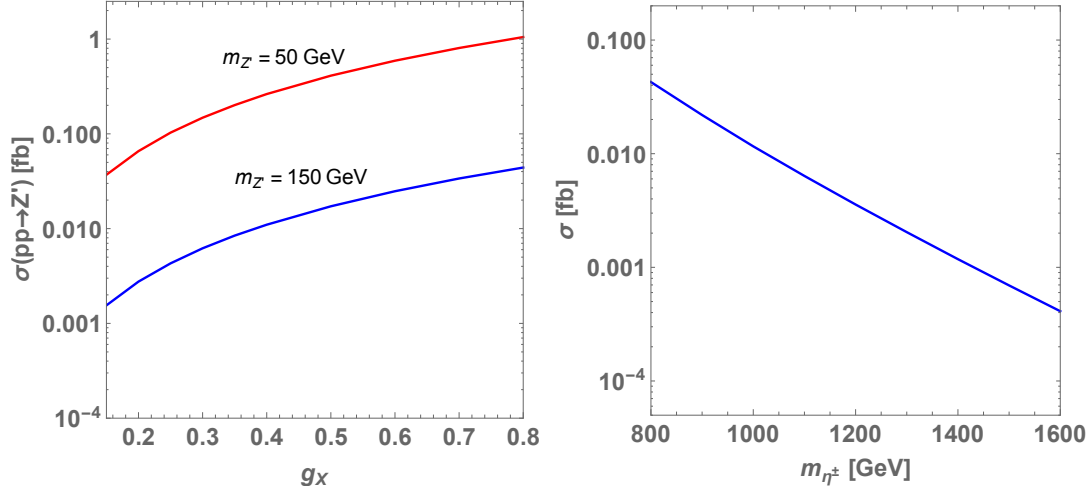


Figure 15. Left: Z' production cross section at the LHC 14 TeV as a function of g_X for $m_{Z'} = 50$ and 150 GeV. Right: cross section for $pp \rightarrow \eta_i^+ \eta_i^-$ process as a function of charged inert scalar mass.

XENON1T [10]. From both plots, it is seen that the results of DM-nucleon scattering cross section in the model are still under the constraints of the direct detection.

4.4 Signatures at the LHC

In this subsection, we discuss signatures from Z' and $\eta_i^+ \eta_i^-$ productions at the LHC. According to the Z' couplings to fermions shown in eq. (3.35), it is seen that the Z' gauge boson can be produced via $q\bar{q} \rightarrow Z'$. Since the interesting Z' mass is lower than the electroweak scale, the production cross section is not highly suppressed even though the kinetic mixing parameter ϵ is of the order of 10^{-3} . By implementing relevant interactions in eq. (3.35) into CalcHEP 3.8 [32] and using the result of ϵ in eq. (3.31), we estimate the Z' production cross section as a function of g_X at $\sqrt{s} = 14$ TeV, shown in the left plot of figure 15, where $m_{S_1} = 1000$ GeV, $m_{S_2} = 1100$ GeV, and $m_{\eta_1^\pm} = m_{\eta_2^\pm}$ are applied. For comparison, we consider the cases with $m_{Z'} = 50$ GeV (red) and 150 GeV (blue). It is found that the cross section is sizable when Z' is light and g_X is as large as the $SU(2)_L$ gauge coupling. After the production, Z' boson decays into the SM fermions (except for the top quarks) whose partial decay widths are:

$$\Gamma(Z' \rightarrow f\bar{f}) = \frac{(C_L^f)^2 + (C_R^f)^2}{24\pi} m_{Z'}, \quad (4.9)$$

where the fermion mass is neglected. Accordingly, the various branching ratios for $m_{Z'} = 50(150)$ GeV can be estimated to be:

$$\begin{aligned} BR(Z' \rightarrow \ell^+ \ell^-) &\simeq 0.28 \text{ (0.26)}, & BR(Z' \rightarrow jj) &\simeq 0.70 \text{ (0.57)} \\ BR(Z' \rightarrow \bar{\nu}\nu) &\simeq 0.02 \text{ (0.17)}, \end{aligned} \quad (4.10)$$

where ℓ^\pm denotes all charged leptons, j indicates jet including b-quark, and $BR(Z' \rightarrow \bar{\nu}\nu)$ includes three generations of neutrino. Note that the branching ratio to neutrino pairs is

suppressed for $m_{Z'} < m_Z$ because the Z' -fermion coupling tends to be dark photon-like. Hence, with $g_X = 0.3$ and $m_{Z'} = 50 \text{ GeV}$, we obtain $\sigma(Z') \times BR(Z' \rightarrow \ell^+ \ell^-) \sim 0.03 \text{ fb}$, in comparison with the upper limit reported by CMS being around 10 fb [33]. Using an integrated luminosity of 3000 fb^{-1} in High-Luminosity (HL) LHC experiments, we can have ~ 90 events for the lepton pair production.

The $\eta_i^+ \eta_i^-$ pairs can be produced via electroweak gauge interactions at the LHC, such as $pp \rightarrow Z^*/\gamma^* \rightarrow \eta_i^+ \eta_i^-$.¹ Using the gauge couplings given in eq. (2.16), the $\eta_i^+ \eta_i^-$ production cross section as a function of η_i^\pm mass is shown in the right plot of figure 15, where we have taken $m_{\eta^\pm} = m_{\eta_1^\pm} = m_{\eta_2^\pm}$. It can be seen that the resulting cross section can reach 0.01 fb at $m_{\eta^\pm} = 1 \text{ TeV}$. Using an integrated luminosity of 137 fb^{-1} at $\sqrt{s} = 13 \text{ TeV}$, the production cross section of chargino pairs is bounded by CMS to be less than 30 fb when the chargino and neutralino masses are 1 TeV and 200 GeV , respectively [34]. If we take the chargino pair measurement as the upper bound of our η_i^\pm pair, the obtained $\sigma(\eta_i^+ \eta_i^-)$ is lower than the current experimental limit. Since $\eta_i^\pm \rightarrow \ell^\pm N$ is the dominant decay channel, to search for the inert charged Higgs boson we can use the signal of dilepton plus missing energy, i.e., $\ell_1^+ \ell_2^- \cancel{E}_T$, similar to the chargino decaying into neutralino, i.e., $\tilde{\chi}^\pm \rightarrow \tilde{\chi}^0 W^\pm$, in the supersymmetric model framework.

Since the significance analysis of the above-mentioned channels involves detailed event simulations with appropriate kinematic cuts beyond the current topic, we leave it to a more dedicated study in the future.

5 Summary and discussions

Based upon the concept of radiative neutrino mass in scotogenic model proposed in [1], we have studied the possibility for the Majorana neutrino mass to arise from an unbroken Stueckelberg $U(1)_X$ gauge model. It is found that although we need two inert Higgs doublets to generate the neutrino mass, just one extra vector-like singlet fermion is sufficient to fit the neutrino data while in contrast at least two right-handed singlet fermions are required in the Ma model. Using the proposed model, we have studied its implications on the low-energy lepton flavor violating (LFV) processes.

We have found that in the model, the resulting $BR(\mu \rightarrow e\gamma)$ can fit the currently experimental upper limit. However, the planned sensitivities of the experiments on the $\mu - e$ conversion and the $\mu \rightarrow 3e$ decay in COMET/Mu2e and Mu3e can cover most of the parameter space that can lead to $BR(\mu \rightarrow e\gamma) \sim 6 \times 10^{-14}$, the designed sensitivity of MEG II experiment. Hence, the $\mu - e$ conversion in nuclei and $\mu \rightarrow 3e$ will be the most promising processes to detect the new physics in the $\mu \rightarrow e$ transitions.

In heavy lepton decays, although the predicted $BR(\tau \rightarrow e\gamma)$ and $BR(\tau \rightarrow 3e)$ are lower than $O(10^{-9})$ and $O(10^{-10})$, the branching ratios for $\tau \rightarrow \mu\gamma$ and $\tau \rightarrow 3\mu$ in the model can cover the range from $O(10^{-8})$ to $O(10^{-9})$ and $O(10^{-10})$, respectively, and can be probed by Belle II experiment.

¹Contribution from the Z' interaction is negligibly small since it is suppressed by the kinetic mixing factor.

We have discussed the dark matter (DM) phenomenology, including estimates of the relic density and the DM-nucleon scattering cross section for the DM mass in the range of 100 GeV to 1 TeV. The relic density has been estimated for two cases: (i) the Z' interaction is dominant (ii) the Yukawa interaction is dominant. In case (i), the observed relic density can be explained with $0.2 \lesssim g_X \lesssim 0.7$ when DM annihilates into $Z'Z'$ while a larger gauge coupling is required when DM pairs annihilate into the SM particles via the s -channel Z' exchange. In case (ii), we make use of the parameter sets obtained from neutrino oscillation observations and flavor-changing constraints. We find that the relic density can be explained by a DM mass less than around 650 GeV. The DM-nucleon cross section is obtained by considering the Z' exchange process and evaluated by fixing some parameters. We have found that it is possible to avoid constraints from direct detection while satisfying the relic density by properly choosing the gauge coupling and Z' mass.

Finally, we have made a brief discussion about the phenomenology of the model at the LHC. In our model, the Z' boson can be produced via kinetic mixing induced at the one-loop level. We have estimated the Z' production cross section and found some number of events can be expected at the HL-LHC. In addition, we have discussed the production of new charged scalar bosons $pp \rightarrow Z^*, \gamma^* \rightarrow \eta_i^+ \eta_i^-$ that lead to the signal of $\ell_1^+ \ell_2^- \cancel{E}_T$. Besides, we have other types of scalar production processes: (i) $pp \rightarrow Z \rightarrow S_i A_i$ and (ii) $pp \rightarrow W^\pm \rightarrow \eta_i^\pm S_i / A_i$. Process (i) unfortunately leads to completely missing energy and cannot trigger the detector because both S_i and A_i decay into neutrinos and DM. The process in case (ii) results in the final state of a charged lepton and missing energy. The transverse mass distribution of the charged lepton here can be used to extract the masses of $\eta_{1,2}^\pm$ as well. Moreover, several SM-like Higgs decays can be modified in the model, such as the $h \rightarrow \gamma\gamma, Z\gamma$ through the $\eta_{1,2}^\pm$ loops and $h \rightarrow \ell^+ \ell^-$ through the loops involving $\eta_{1,2}^\pm$ and N . Of a different topic from the current work, a detailed examination of the above-mentioned collider phenomenology will be deferred to a more dedicated study.

Acknowledgments

This work was supported in part by the Ministry of Science and Technology, Taiwan under the Grant Nos. MOST-110-2112-M-006-010-MY2, MOST-108-2112-M-002-005-MY3, and MOST-111-2112-M-002-018-MY3. The work is also supported by the Fundamental Research Funds for the Central Universities (T. N.).

Open Access. This article is distributed under the terms of the Creative Commons Attribution License ([CC-BY 4.0](https://creativecommons.org/licenses/by/4.0/)), which permits any use, distribution and reproduction in any medium, provided the original author(s) and source are credited. SCOAP³ supports the goals of the International Year of Basic Sciences for Sustainable Development.

References

- [1] E. Ma, *Verifiable radiative seesaw mechanism of neutrino mass and dark matter*, *Phys. Rev. D* **73** (2006) 077301 [[hep-ph/0601225](#)] [[INSPIRE](#)].

- [2] PLANCK collaboration, *Planck 2018 results. VI. Cosmological parameters*, *Astron. Astrophys.* **641** (2020) A6 [Erratum *ibid.* **652** (2021) C4] [[arXiv:1807.06209](#)] [[INSPIRE](#)].
- [3] MEG II collaboration, *The design of the MEG II experiment*, *Eur. Phys. J. C* **78** (2018) 380 [[arXiv:1801.04688](#)] [[INSPIRE](#)].
- [4] C.M. Perez and L. Vigani, *Searching for the Muon Decay to Three Electrons with the Mu3e Experiment*, *Universe* **7** (2021) 420 [[INSPIRE](#)].
- [5] COMET collaboration, *COMET Phase-I Technical Design Report*, *PTEP* **2020** (2020) 033C01 [[arXiv:1812.09018](#)] [[INSPIRE](#)].
- [6] E. Diociaiuti, $\mu \rightarrow e$ conversion and the Mu2e experiment at Fermilab, *PoS EPS-HEP2019* (2020) 232 [[INSPIRE](#)].
- [7] R.J. Barlow, *The PRISM/PRIME project*, *Nucl. Phys. B Proc. Suppl.* **218** (2011) 44 [[INSPIRE](#)].
- [8] A.Y. Bai et al., *Snowmass2021 Whitepaper: Muonium to antimuonium conversion*, [arXiv:2203.11406](#) [[INSPIRE](#)].
- [9] J. Leite, A. Morales, J.W.F. Valle and C.A. Vaquera-Araujo, *Scotogenic dark matter and Dirac neutrinos from unbroken gauged $B - L$ symmetry*, *Phys. Lett. B* **807** (2020) 135537 [[arXiv:2003.02950](#)] [[INSPIRE](#)].
- [10] XENON collaboration, *Dark Matter Search Results from a One Ton-Year Exposure of XENON1T*, *Phys. Rev. Lett.* **121** (2018) 111302 [[arXiv:1805.12562](#)] [[INSPIRE](#)].
- [11] BELLE-II collaboration, *The Belle II Physics Book*, *PTEP* **2019** (2019) 123C01 [Erratum *ibid.* **2020** (2020) 029201] [[arXiv:1808.10567](#)] [[INSPIRE](#)].
- [12] A. Merle and M. Platscher, *Parity Problem of the Scotogenic Neutrino Model*, *Phys. Rev. D* **92** (2015) 095002 [[arXiv:1502.03098](#)] [[INSPIRE](#)].
- [13] T. Toma and A. Vicente, *Lepton Flavor Violation in the Scotogenic Model*, *JHEP* **01** (2014) 160 [[arXiv:1312.2840](#)] [[INSPIRE](#)].
- [14] S. Weinberg, *Baryon and Lepton Nonconserving Processes*, *Phys. Rev. Lett.* **43** (1979) 1566 [[INSPIRE](#)].
- [15] J. Hisano, T. Moroi, K. Tobe and M. Yamaguchi, *Lepton flavor violation via right-handed neutrino Yukawa couplings in supersymmetric standard model*, *Phys. Rev. D* **53** (1996) 2442 [[hep-ph/9510309](#)] [[INSPIRE](#)].
- [16] Y. Kuno and Y. Okada, *Muon decay and physics beyond the standard model*, *Rev. Mod. Phys.* **73** (2001) 151 [[hep-ph/9909265](#)] [[INSPIRE](#)].
- [17] E. Arganda, M.J. Herrero and A.M. Teixeira, μ - e conversion in nuclei within the CMSSM seesaw: Universality versus non-universality, *JHEP* **10** (2007) 104 [[arXiv:0707.2955](#)] [[INSPIRE](#)].
- [18] T.S. Kosmas, S. Kovalenko and I. Schmidt, *Nuclear $\mu^- e^-$ conversion in strange quark sea*, *Phys. Lett. B* **511** (2001) 203 [[hep-ph/0102101](#)] [[INSPIRE](#)].
- [19] R. Conlin and A.A. Petrov, *Muonium-antimuonium oscillations in effective field theory*, *Phys. Rev. D* **102** (2020) 095001 [[arXiv:2005.10276](#)] [[INSPIRE](#)].
- [20] L. Willmann et al., *New bounds from searching for muonium to anti-muonium conversion*, *Phys. Rev. Lett.* **82** (1999) 49 [[hep-ex/9807011](#)] [[INSPIRE](#)].

- [21] K.S. Babu, C.F. Kolda and J. March-Russell, *Implications of generalized Z - Z' mixing*, *Phys. Rev. D* **57** (1998) 6788 [[hep-ph/9710441](#)] [[INSPIRE](#)].
- [22] I. Esteban, M.C. Gonzalez-Garcia, M. Maltoni, T. Schwetz and A. Zhou, *The fate of hints: updated global analysis of three-flavor neutrino oscillations*, *JHEP* **09** (2020) 178 [[arXiv:2007.14792](#)] [[INSPIRE](#)].
- [23] M.C. Gonzalez-Garcia, M. Maltoni and T. Schwetz, *NuFIT: Three-Flavour Global Analyses of Neutrino Oscillation Experiments*, *Universe* **7** (2021) 459 [[arXiv:2111.03086](#)] [[INSPIRE](#)].
- [24] SINDRUM II collaboration, *Test of lepton flavor conservation in $\mu \rightarrow e$ conversion on titanium*, *Phys. Lett. B* **317** (1993) 631 [[INSPIRE](#)].
- [25] PARTICLE DATA GROUP collaboration, *Review of Particle Physics*, *PTEP* **2020** (2020) 083C01 [[INSPIRE](#)].
- [26] MUON G-2 collaboration, *Measurement of the Positive Muon Anomalous Magnetic Moment to 0.46 ppm*, *Phys. Rev. Lett.* **126** (2021) 141801 [[arXiv:2104.03281](#)] [[INSPIRE](#)].
- [27] S. Borsányi et al., *Leading hadronic contribution to the muon magnetic moment from lattice QCD*, *Nature* **593** (2021) 51 [[arXiv:2002.12347](#)] [[INSPIRE](#)].
- [28] G. Bélanger, F. Boudjema, A. Pukhov and A. Semenov, *MicrOMEGAs4.1: two dark matter candidates*, *Comput. Phys. Commun.* **192** (2015) 322 [[arXiv:1407.6129](#)] [[INSPIRE](#)].
- [29] FERMI-LAT collaboration, *Searching for Dark Matter Annihilation from Milky Way Dwarf Spheroidal Galaxies with Six Years of Fermi Large Area Telescope Data*, *Phys. Rev. Lett.* **115** (2015) 231301 [[arXiv:1503.02641](#)] [[INSPIRE](#)].
- [30] FERMI-LAT and DES collaborations, *Searching for Dark Matter Annihilation in Recently Discovered Milky Way Satellites with Fermi-LAT*, *Astrophys. J.* **834** (2017) 110 [[arXiv:1611.03184](#)] [[INSPIRE](#)].
- [31] A. Alves, A. Berlin, S. Profumo and F.S. Queiroz, *Dark Matter Complementarity and the Z' Portal*, *Phys. Rev. D* **92** (2015) 083004 [[arXiv:1501.03490](#)] [[INSPIRE](#)].
- [32] A. Belyaev, N.D. Christensen and A. Pukhov, *CalcHEP 3.4 for collider physics within and beyond the Standard Model*, *Comput. Phys. Commun.* **184** (2013) 1729 [[arXiv:1207.6082](#)] [[INSPIRE](#)].
- [33] CMS collaboration, *Search for a Narrow Resonance Lighter than 200 GeV Decaying to a Pair of Muons in Proton-Proton Collisions at $\sqrt{s} = 13$ TeV*, *Phys. Rev. Lett.* **124** (2020) 131802 [[arXiv:1912.04776](#)] [[INSPIRE](#)].
- [34] CMS collaboration, *Search for electroweak production of charginos and neutralinos at $\sqrt{s} = 13$ TeV in final states containing hadronic decays of WW , WZ , or WH and missing transverse momentum*, [arXiv:2205.09597](#) [[INSPIRE](#)].